A Two-Way Coupling Approach for Simulating Bouncing Droplets

Hui Wang[1] | Yuwei Xiao[1] | Yankai Mao[1] | Shiying Xiong[2] | Xubo Yang[1] | Bo Zhu[3]

[1]Shanghai Jiao Tong University, Shanghai, 200240, China

[2]Zhejiang University, Hangzhou, 310058, China

[3]Georgia Institute of Technology, Atlanta, GA 30332, United States

Correspondence
Author One PhD, Department, Institution, City, State or Province, Postal Code, Country
Email: wanghehv@sjtu.edu.cn

Funding information

This paper presents a two-way coupling approach to simulate bouncing droplet phenomena by incorporating the lubricated thin aerodynamic gap between fluid volumes. At the heart of our framework lies a cut-cell representation of the thin air film between colliding liquid fluid volumes. The air pressures within the thin film, modeled using a reduced fluid model based on the lubrication theory, are coupled with the volumetric liquid pressures by the gradient across the liquid-air interfaces and solved in a monolithic two-way coupling system. Our method can accurately solve liquid-liquid interaction with air films without adaptive grid refinements, enabling accurate simulation of many novel surface-tension-driven phenomena such as droplet collisions, bouncing droplets, and promenading pairs.

KEYWORDS

fluid-fluid contact, surface tension flow, multi-phase fluid, cut-cell, thin film, walking droplet

1 | INTRODUCTION

When fluid volumes get small, i.e., on the length scales between $O(0.1)$ μm – $O(1)$ mm, their interactions exhibit complicated flow dynamics and geometric forms governed by many small-scale physical processes. For instance, a fluid volume can collide and bounce [1], walk [2, 3], wrap [4, 5, 6], glide [7], support and drive [8], or form non-manifold geometric structures [9, 10]. These flow processes are remarkably different from their macroscopic counterparts, be-

having like deformable solids (e.g., a fluid surface can hold heavy objects, and fluid volumes can collide and bounce) rather than shear irresistible liquids. A dominant force underpinning these small-scale flow processes is surface tension. The recent advances in computational physics [11, 12, 13, 14, 15, 16] and computer graphics [17, 18, 19, 6, 20] in devising algorithms to accurately simulate surface tension with complex geometries and multi-physics interactions have enabled numerical explorations of an ensemble of new interfacial and solid-fluid coupling phenomena that were impractical to simulate with traditional methods.

However, among these new surface-tension phenomena being tackled, devising first-principle approaches to model the intricate interactions between droplets and fluid volumes remains challenging due to the difficulties of handling the multi-phase and multi-scale coupling. When a small droplet falls onto a pond surface, it could rebound, decrease its size, and sit on the deforming surface for seconds long, before its eventual merge into the water bulk (e.g., see [21, 22, 23]). The physical mechanics underpinning this seemingly discrete phenomenon lie in the evolution of a thin air gap between the droplet and the liquid surface. When two fluid volumes approach each other, a thin layer of the surrounding air is trapped in the narrow gap between them [24, 21]. As the air gap's thickness decreases, the air viscosity dominates its dynamics according to the lubrication theory, which leads to the resistance of air drainage and prevents the liquids from merging together. As the air leaks out, the gap narrows to a point where it can no longer maintain the separation of the liquids, eventually leading to their coalescence [21]. Intuitively speaking, the dynamics of the thin gap acts as an air cushion transmitting pressure forces between the liquid volumes and coupling their interfacial dynamics without exhibiting any liquid-liquid contact. During the process, the air gap's thickness scale is $O(0.1)$ μm, in comparison to $O(1)$ mm as the droplet size.

This multiphase and multiscale coupling problem underpins many droplets splashing, adhesion, and walking droplet phenomena [22], which has drawn extensive attention from experimental and theoretical physicists. In the literature, the rebound behavior of droplets in the binary collision was first reported by Rayleigh [25] and analyzed by Pan et al. [1], Zhang and Law [26]. Similar rebound phenomena have also been observed when droplets bounced on the soap films [27], rigid surfaces [28, 29] and liquid surfaces [24]. Among these works, Couder et al. [21] reported the role of air film in the process of droplet bouncing. Further studies show that droplets can interact with liquid in different ways, including walking [30, 2, 3], diffraction and interference [31], tunneling across the submerged barrier [32], and orbiting [33, 34]. Bush [35] summarized these quantum-style behaviors and connected the hydrodynamics system with the quantum theories. The quantum analogs also emerge in multi-droplet scenarios, including orbiting pairs [36, 37], promenading pairs [38], stable spin lattices [39], droplet rings [40]. The experimental studies and theoretical models for quantum analogs are reviewed and summarized in [41].

From the perspective of the numerical simulation, thin fluids, such as sheets [42, 43], splashes [44, 45], bubbles [46, 47, 48], films [49, 50, 20], as well as air gaps discussed above, all exhibit codimensional geometric features that are challenging to resolve with a traditional volumetric discretization (e.g., a Cartesian grid or a simplicial mesh). To capture these thin fluid features, researchers invented a broad range of hybrid geometric representations, such as particles [51, 52, 20], surface meshes [53, 10, 47, 43], implicit interfaces [46, 54, 55], and hybrid particle-grid representation [42, 19]. By tracking the geometry changes and assigning degrees of freedom to the thin structures, these representations enable us to discretize and effectively solve the physical forces acting on codimensional structures. Moreover, these codimensional representations allow researchers to simplify the physical models further. For instance, in the context of modeling bouncing droplets, recent works [56, 57, 13, 58, 59] employ a reduced lubrication film model to resolve the thin air flow within the gaps by considering the tangential viscosity as the primary force.

Cut-cell methods (e.g., [60, 61, 62]) provide an effective alternative for modeling thin features while keeping the uniform grid structure. In contrast to adaptive mesh refinement (AMR) methods [63, 64, 12], which recursively refine the grid to achieve sufficient resolution on thin features, cut-cell methods divide an interface cell with fine geometries

66 and evaluate the flow details with additional degrees of freedom. Its main advantage over dedicated codimensional
67 modeling is that it offers a straightforward and intuitive way to integrate the thin features with their surrounding
68 volumetric domains. These methods are commonly employed in simulating the thin gap flow [65, 66], multiphase
69 fluids [67], fluid-rigid interaction [60, 61, 68], and fluid-deformable interactions [69]. E.g., Chen et al. [70] improves
70 cut-cell methods by incorporating a pressure reposition strategy, resulting in second-order accuracy and discretization
71 orthogonality. When it comes to thin-gap flow, Qiu et al. [65] solved a two-way coupling system between thin gaps and
72 solids, where additional pressure degrees of freedom were placed on the solid surface. Another category of research
73 strives to capture the sub-cell flow details by integrating the irregular cell into the Eulerian framework, including
74 Voronoi cells [71, 72], tetrahedral cells [73] and tilted cells [74].

75 We propose a novel two-way coupling approach to simulate the bouncing droplet phenomena based on first
76 principles. Our algorithm couples fluid volumes, thin air gaps, and interfacial forces in a monolithic manner to model
77 the aerodynamics-driven fluid contact processes by producing simulations that match real-world experiments in three-
78 dimensional settings. Our key idea is to discretize the air gap as a set of irregular grid cells and devise a reduced
79 fluid model to characterize their coupling with the liquid volumes. Our method creates a new set of irregular grid
80 cells specified with varying thicknesses that can be embedded in a Cartesian grid to characterize the thin air film.
81 This novel geometric representation captures the air-liquid interactions within a thin gap with an arbitrary thickness
82 without employing any adaptivity (which is impractical in this setting due to the drastically different length scales). On
83 top of this novel geometric discretization, we further build a monolithic system to solve the coupling problem.

84 We demonstrate the effectiveness of our approach by simulating different bouncing droplet phenomena involv-
85 ing thin intervening air films. These phenomena include binary collision, bouncing droplets, promenading pairs, and
86 droplet pinch-off. We also validate the accuracy of our model by comparing the simulation results with experimen-
87 tal videos in different collision and contact settings. Our method enables three-dimensional simulations of bouncing
88 droplets that match real-world physics, and it produces visually authentic animations to demonstrate these compli-
89 cated processes. We summarize the main contributions of our work as:

90 • A discrete representation to model aerodynamic thin films with varying thicknesses as the single-layered irregular
91 cells.
92 • A cut-cell grid method to couple multiphase fluids with contrasting length scales.
93 • A monolithic coupling algorithm to solve the lubricated air film and incompressible flow in a single linear solve.
94 • A unified simulation framework to simulate bouncing droplets with physical accuracy.

95 This paper is organized as follows. In Section 2, we present the physical model of the system. Section 3 introduces
96 the geometrical discretization and defines the differential operators on the cut-cell liquid regions and the single-layer
97 irregular air cells. We then proceed to build a coupling system to resolve the pressure across the volumetric liquid
98 regions and the lubricated air film in Section 4. In Section 5, we outline our temporal evolution scheme and introduce
99 the remaining steps of the algorithm. The results of the numerical validation and the simulation are presented in
100 Section 6. Finally, we conclude our work and discuss the limitations and future directions in Section 7.
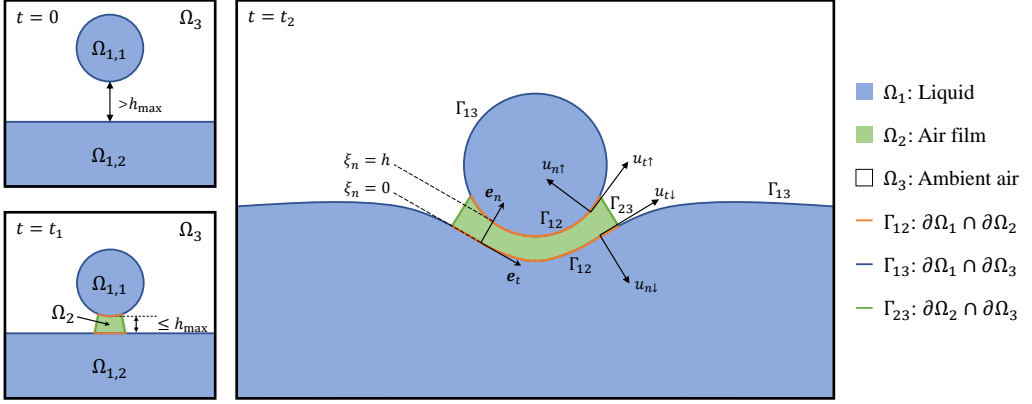
FIGURE 1 *Illustration of fluid domains and interfaces*. The entire computational domain is divided into three domains. Ω_1 is liquid, Ω_2 is the thin air film, and Ω_3 is ambient air. Interfaces are denoted using the corresponding subscripts (Γ_{12}, Γ_{13}, Γ_{23}). We show examples of the domain evolution at $t = \{0, t_1, t_2\}$. *Left Top:* When $t = 0$, a droplet $\Omega_{1,1}$ is released above the liquid bath $\Omega_{1,2}$. The distance between two liquid volumes is more significant than a predefined film thickness threshold h_{max}. *Left Bottom:* When $t = t_1$, the liquid volumes approach each other. The thin air film Ω_2 is identified where the distance between two liquids is less than h_{max}. *Right:* When $t = t_2$, the liquid bath deforms due to the impact of the droplet. In the air film, we define local coordinates on $\Gamma_{12} \cap \partial\Omega_{1,2}$ as a tangential basis vector e_t and a normal basis vector e_n. The local coordinates are parameterized by ξ_t and ξ_n. The local thickness h of the air film at $x \in \Gamma_{12} \cap \partial\Omega_{1,j}$ is approximated as its distance to $\Omega_{1,k}$. $u_{t\uparrow}, u_{t\downarrow}$ specify the local tangential velocities on the upper and down sides of air film (both denoted as Γ_{12}). Similarly, $u_{n\uparrow}, u_{n\downarrow}$ specify the local normal velocities on the two sides.

2 | PHYSICAL MODEL

2.1 | Domain Definition

As shown in Figure 1, we use $\Omega = \Omega_1 \cup \Omega_2 \cup \Omega_3 \cup \Gamma$ to denote the entire fluid domain. In particular, we use Ω_1 to represent liquid volumes (including both bulks and droplets), Ω_2 to represent the thin air film, and Ω_3 to represent ambient air. The liquid domain Ω_1 can be further divided into liquid volumes ($\Omega_{1,j}, j \in \mathbb{N}^*$) (e.g., liquid bath and bouncing drops) according to their topological connectivities. The thin air film Ω_2 is defined as the region where the distance between two liquid volumes is less than a predefined thickness threshold h_{max}. Mathematically, this film can be featured as $\Omega_2 = \{x \in \Omega : x \notin \Omega_1 \text{ and } d(x, \Omega_{1,j}) + d(x, \Omega_{1,k}) \leq h_{max} \text{ with } j \neq k\}$, where $d(x, \Omega_{1,j}) = \min_{\tilde{x}\in\Omega_{1,j}} (|x - \tilde{x}|)$ returns the distance between x and $\Omega_{1,j}$. In addition to Ω, we use Γ to denote the fluid interface across different domains. We let $\Gamma = \Gamma_{12} \cup \Gamma_{23} \cup \Gamma_{13}$, where Γ_{12} is the interface between Ω_1 and Ω_2, $\Gamma_{13} = \partial\Omega_1 \setminus \Gamma_{12}$ is the interface between liquid and ambient air and $\Gamma_{23} = \partial\Omega_2 \setminus \Gamma_{12}$ is the interface between thin film and ambient air.

2.2 | Volumetric, Multiphase Fluid Model

We model the motion of fluid volumes by solving the multiphase, incompressible Navier–Stokes equations

$$
\begin{cases}
\dfrac{\partial \boldsymbol{u}}{\partial t} + \boldsymbol{u} \cdot \boldsymbol{\nabla} \boldsymbol{u} = -\dfrac{\boldsymbol{\nabla} p_i}{\rho_i} + \dfrac{\mu_i}{\rho_i}\nabla^2 \boldsymbol{u} + \boldsymbol{g}, \\
\boldsymbol{\nabla} \cdot \boldsymbol{u} = 0,
\end{cases}
\quad \boldsymbol{x} \in \Omega_i, \ \ i = 1,2,3
\tag{1}
$$

with the interface jump conditions

$$
\begin{cases}
[p_1] = \gamma\kappa, \ \ \boldsymbol{x} \in \Gamma_{12} \cup \Gamma_{13}, \\
[p_2] = 0, \ \ \boldsymbol{x} \in \Gamma_{23}, \\
[\boldsymbol{u}] = 0, \ \ \boldsymbol{x} \in \Gamma_{12} \cup \Gamma_{13} \cup \Gamma_{23},
\end{cases}
\tag{2}
$$

where $\boldsymbol{u}$ is the velocity, $\boldsymbol{g}$ is the gravitational acceleration, p_i is the pressure in Ω_i, γ is the surface tension coefficient, and κ is the local mean curvature. $[\cdot]$ denotes the jump condition across an interface.

Solving Equation (1) on a Cartesian grid directly is impractical, due to the vanishingly small domain thickness of the air gap. Therefore, we exercise simplification in each domain. For the liquid domain Ω_1, we drop the viscosity term. For the ambient air domain Ω_3, we assume the air pressure is constant, i.e., $p_3 = p_{atm}$, where p_{atm} is the default atmospheric pressure. The model simplification of thin-film flow is nontrivial, which we will discuss next.

2.3 | Thin-film Fluid Model

We model the trapped air between fluid volumes as a lubricated thin film of air volume. We will first describe its geometry model and then present the dynamics equations.

2.3.1 | Thin-film geometry

Due to the extremely thin nature of the trapped air between fluid volumes, conventional grid methods struggle to track it efficiently. Recent advancements [58, 13] have proposed simplifying the air film model to single-layered Degrees of Freedom (DoF) with varying thicknesses. These DoFs are defined and solved only within a limited range, where the thickness remains below a certain threshold. Such simplification enables efficient tracking and accurate reproduction of head-on collisions of droplets. Our approach takes this idea further by integrating it with a standard Eulerian grid, facilitating more intricate interactions between liquids and the trapped air film. We model trapped air on a thin film with spatially varying thickness between the fluid volumes. Next, we discuss its geometry model and parameterization.

For geometry description, we model a thin layer of air as a codimension-1, open surface with varying thickness embedded in codimension-0 space. The two sides of the surface are the two interfaces between different fluid volumes in Ω_1 and the air film Ω_2. The open boundary of the surface (as a codimension-2 rim) is the interface between the air film Ω_2 and the ambient Ω_3.

For surface parameterization, we define a local coordinate system at each point of the surface by establishing a set of orthonormal basis vectors. For example, as shown in Figure 1, in two-dimensional space, we define $\boldsymbol{e}_t$ and $\boldsymbol{e}_n$ according to the local geometry as the tangential and normal basis vectors. A point in the air film can be described using its coordinates ξ_t and ξ_n. These definitions can be naturally extended to three-dimensional cases. For each local

141 point within the film, we define its local thickness h as the sum of distances to two adjacent liquid volumes.

142 ## 2.3.2 | Thin-film dynamics

143 Next, we will derive the governing equations for thin-film airflow based on Equation (1). We will first present the
144 differential form and then the integral form.

145 **Differential form**

146 According to [58, 13, 12], in scenarios where droplets exhibit bouncing behaviors, the pressure increase within the
147 film is relatively small due to the low collision velocity. Therefore, the incompressible assumption within the air film is
148 deemed acceptable for reproducing the desired phenomena. We adopt this simplification, following previous works,
149 by modeling the air film as an incompressible fluid.

150 Following [75, 58], we reduce Equation (1) by modeling the normal and tangent gradients of air pressure in the
151 thin film as

$$\begin{cases} \dfrac{\partial p_2}{\partial \xi_t} = \mu_2 \dfrac{\partial^2 u_t}{\partial \xi_n^2}, \\ \dfrac{\partial p_2}{\partial \xi_n} = 0, \end{cases} \quad x \in \Omega_2, \tag{3}$$

152 with

$$\begin{cases} [p_2] = -\gamma\kappa, & x \in \Gamma_{12}, \\ [p_2] = 0, & x \in \Gamma_{23}, \end{cases} \tag{4}$$

153 where ξ_n and ξ_t denote the local unit normal and tangent directions, respectively, and u_n, u_t are normal and tangent
154 components of the air velocity, respectively. The intuition behind Equation (3) is as follows: As the thickness of the
155 air film decreases, especially when the thickness is much smaller than the characteristic tangent length, the viscosity
156 drag becomes the dominant force [76, 75].

157 **Integral form**

158 Based on Equation (3), we can further derive the integral form for thin-film flow. Given a small control volume V
159 in the air film, we define its tangent volume boundary as ∂V_t and its normal volume boundary as $\partial V_n \subseteq \Gamma_{12}$. The
160 pressure within V is governed by the incompressibility constraints in Equation (1), where the sum of the integrated
161 flux through the boundary is zero. By substituting the lubrication model into the tangent flux on ∂V_t and considering
162 the pressure-gradient force on the normal boundary ∂V_n, the air-film pressure takes the form

$$\int_{\partial V_t} \frac{h^2}{12\mu} \frac{\partial p_2}{\partial \xi_t} ds + \Delta t \int_{\partial V_n} \frac{1}{\rho_2} \frac{\partial p_2}{\partial \xi_n} ds = \int_{\partial V_t} \frac{u_{t\uparrow} + u_{t\downarrow}}{2} ds + \int_{\partial V_n} u_n ds \tag{5}$$

163 with the jump conditions on the interfaces
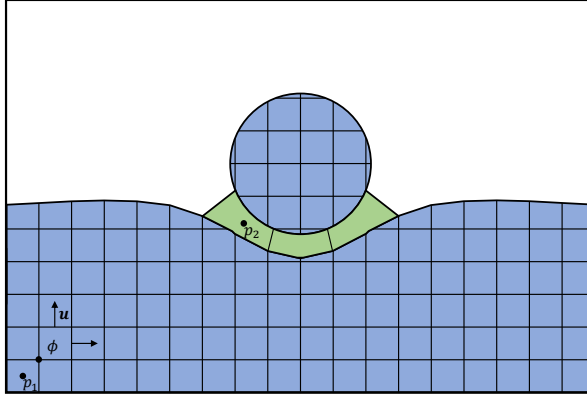
FIGURE 2 *Discretization of liquids and the air film.* The liquid domain Ω_1 (blue) is divided into several separate liquid volumes on the Cartesian grid enhanced by cut-cells, with level set ϕ, pressure p_1 and velocity u sampled on nodes, cells, and faces. In the gap between liquid volumes, the air film Ω_2 (green) is represented by single-layered irregular cells and the cut-cell meshes to solve pressure p_2.

$$\begin{cases} [p_2] = -\gamma\kappa, & x \in \Gamma_{12}, \\ [p_2] = 0, & x \in \Gamma_{23}, \end{cases} \tag{6}$$

where Δt is the time step, $u_{t\uparrow}$, $u_{t\downarrow}$ represent the local tangent boundary velocity evaluated at $\Gamma_{12} \cap \partial\Omega_{1,k}$ and $\Gamma_{12} \cap \partial\Omega_{1,j}$ respectively (see Figure 1), and u_n is the local normal boundary velocity. We refer readers to a detailed derivation in A.
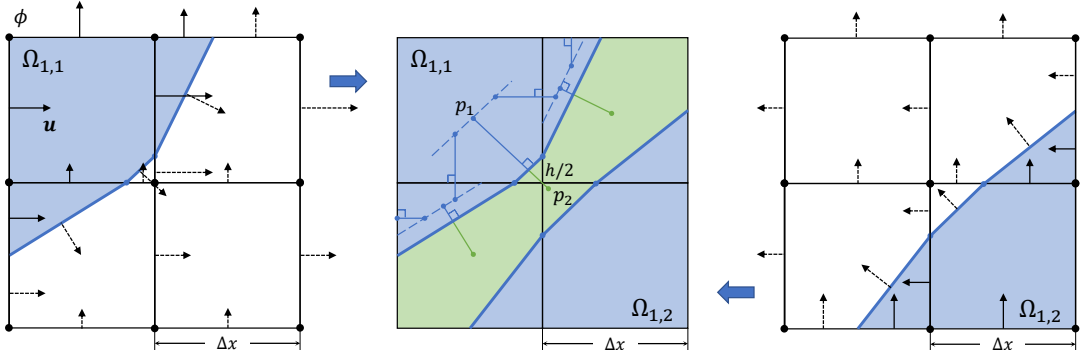
3 | DISCRETIZATION

3.1 | Sub-cell discretization

We discretize the liquid domain Ω_1 as multiple separate liquid volumes on a Cartesian grid with cut cells. Every liquid volume is tracked in a regular background grid by a separate node-based level set. The cut-cell mesh is rebuilt from the level set to represent its interface. The interface grid cells are cut into sub-cells. The pressure samples are repositioned carefully to maintain the orthogonality of the gradient to the cut-cell interface, thus achieving sub-grid accuracy. Based on the cut-cell meshes, the air film Ω_2 is constructed as single-layered irregular cells sandwiched between cut-cell-based liquid volumes, as shown in Figure 2.

3.1.1 | Liquid discretization

We divide the liquid domain Ω_1 into separate regions by running a flood-fill algorithm. As shown in Figure 3, we track each liquid region by creating its own level set function on a regular background grid. We define the interface $\partial\Omega_1$ by constructing a cut-cell isocontour mesh using the marching cubes algorithm [77]. Specifically, to find the intersection

FIGURE 3 *Discretization of the liquid level set, velocity, and pressure.* We split the liquid domain into multiple liquid regions ($\Omega_{1,1}$, $\Omega_{1,2}$, ...). *Left* and *Right*: Each region has its own node-based level set ϕ (black dots) and face-based velocity field u (solid arrows). The interfaces $\partial\Omega_1$ are discretized into the cut-cell mesh (blue segments) by performing the marching cubes algorithm on level sets. The velocity fields are sampled on grid faces (solid arrows) and extrapolated (dashed arrows). *Middle*: When coupling fluid regions with the air film (green), the normal velocities on the cut faces (dashed arrows) are interpolated from the grid faces. The pressure samples (blue dots) in the cut-cell are repositioned on the same iso-distance (blue dotted lines) parallel to the interface, following [70].

between an interface and a grid edge, we check the sign change of the level set on the grid edge. These intersections, called *cut vertices*, can be expressed mathematically as $x = (1-\theta)x_l + \theta x_m$ with $\theta = \phi(x_l)/(\phi(x_l) - \phi(x_m))$, where x_l and x_m are the two endpoints of a grid edge. The cut vertices are then connected into meshes (segment mesh in 2D or triangle mesh in 3D). The faces of this cut-cell mesh are referred to as "*cut faces*" to distinguish them from the regular "*grid faces*".

As illustrated in Figure 3, the velocity field for each liquid volume is split into orthogonal components and stored in grid faces. The interface velocities are sampled at the center of the cut faces and interpolated from the grid faces. Under an inviscid assumption, only the normal component of the interface velocity is preserved.

We follow [70] to reposition the pressure samples along the iso-surface within the cut-cell for improved sub-grid accuracy and discretization orthogonality. By assuming equivalent pressure values along the iso-surface, a single pressure variable for a cut cell can be mapped to multiple pressure samples equidistant to the interface. For each cut-cell, an appropriate iso-distance value is determined, such that the iso-surface intersects with the perpendicular lines of all its grid faces and cut faces through their centroids. These newly generated samples are positioned at these intersection points, guaranteeing that pressure gradients are always orthogonal to cell faces and co-located with velocity samples at those face centroids. The central difference stencils are then constructed based on this discretization. We recommend readers refer to [70] for further details.

In brief, in our discretization, each liquid cell is surrounded by a cut-cell mesh where velocity is defined, encompassing both cut faces and grid faces. The pressure samples are duplicated at multiple locations to facilitate the calculation of differential operators on each face.

3.1.2 | Air-film discretization

The air film Ω_2 is discretized as a set of single-layered irregular cells seamlessly embedded in the thin gap between liquid volumes. These air cells are reconstructed every time step based on the cut-cell mesh of the surrounding liquid
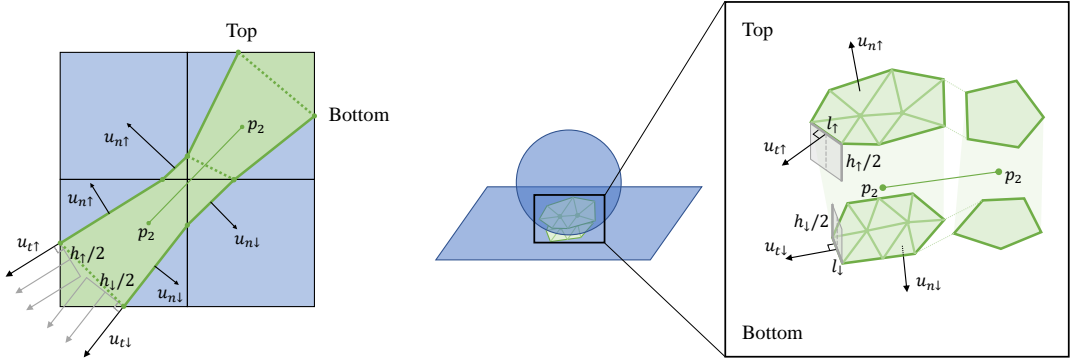
FIGURE 4 *Discretization of the irregular air film cells in 2D (Left) and 3D (Right).* The top and bottom of the air cell are defined by the cut-cell mesh (green faces). The lateral cell boundaries are discretized as half faces at the rim (grey faces). $u_{n\uparrow}$ and $u_{n\downarrow}$ are the normal velocity of interfaces at the center of cut faces interpolated from the liquid volumes. $u_{t\uparrow}$ and $u_{t\downarrow}$ are the tangential velocity interfaces evaluated at the cut vertices in 2D or the midpoints of cut edges in 3D.

volumes. After advection, we construct the cut-cell mesh for liquid volumes and organize the nearby cut faces from different regions into groups. One air cell is then assigned on each cut face group with the cut-meshes serving as its top and bottom surface, as shown in Figure 4. The air pressure degrees of freedom are placed at the center of the cut face groups. More details on the construction of the air film can be found in Section 5.3.

The air-film thickness varies within a single air cell. For an air cell located between liquid volumes $\Omega_{1,j}$ and $\Omega_{1,k}$, given a vertex x on the cut face in $\partial\Omega_{1,j} \cap \Gamma_{12}$, the local thickness h is defined as $\phi_k(x)$ where ϕ_k is the levelset function of the other liquid volume $\Omega_{1,k}$. The thickness of a cut face is defined as the average of its vertices.

The cut-cell meshes, obtained from the interfaces of liquid volumes, also serve as the top and bottom boundaries of air cells. The normal velocities on the top and bottom surfaces $u_{n\uparrow}, u_{n\downarrow}$ are sampled at the center of these cut faces and interpolated from the liquid velocity. However, it is challenging to explicitly define the lateral surface of the air cell using meshes, especially in three-dimensional cases. Instead, we represent the lateral surface with *half faces*, which are the faces expanded from the rim of the top and bottom meshes along the local normal direction.

As shown in Figure 4 (Left), for two-dimensional cases, we define half faces on the rim vertices. These half-faces are half-height lateral faces connected to the top or bottom of air cells and are normal to the local tangent. The area of the half face is approximated as $h_\uparrow/2$ or $h_\downarrow/2$, where $h_\uparrow$, $h_\downarrow$ are the air film thickness evaluated at the top and bottom cut vertices. The tangent velocities on the half faces are interpolated from the liquid volumes at the cut vertices on the rim of the air cell, denoted by $u_{t\uparrow}$ and $u_{t\downarrow}$ respectively. The tangent flux between two air cells is approximated at both top and bottom boundaries as $u_{t\uparrow}h_\uparrow/2 + u_{t\downarrow}h_\downarrow/2$. Note that this boundary tangent flux form is only utilized as the first term on the right-hand side in Equation (5).

In a three-dimensional case, the half faces are defined on the rim edges of the top and bottom meshes, as in Figure 4 (Right). The lateral tangent velocities $u_{t\uparrow}$, $u_{t\downarrow}$ are interpolated at the midpoint of the rim edges, and the lateral area of the half face is $lh/2$ where l is the length of the rim edge. Unlike the two-dimensional case, there is no one-to-one mapping between the half faces on the top and bottom boundaries in the three-dimensional case. To obtain the tangent flux between two air cells, we iterate over the common rim edges between the two cells and sum up the flux of the half faces on these rim edges. With the lateral interfaces of air cells defined on the half faces based on the
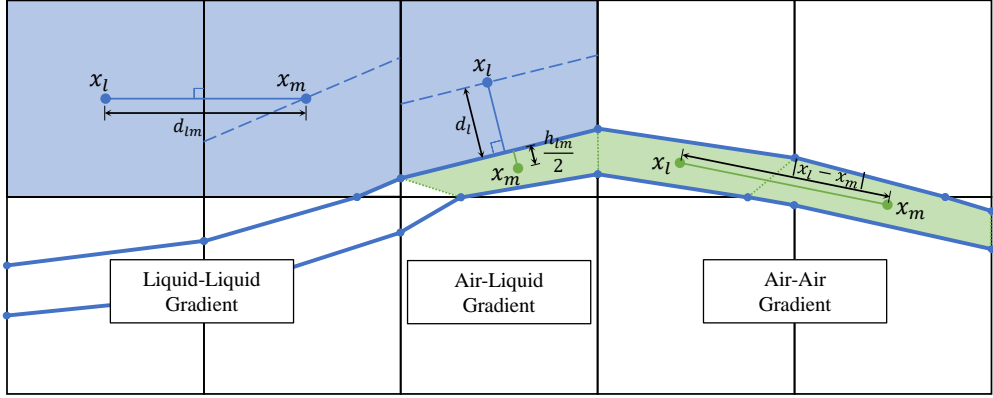
FIGURE 5 *Discretization of three types of gradient operators in 2D.* The three types of discretized gradient operators – liquid-liquid, air-liquid, and air-air – are depicted on the grid. The involved liquid and air cells are colored in blue and green, separately. The pressure DoFs are represented by large dots, while the distances between DoFs utilized in gradient operators are visualized as arrowed lines.

top and bottom boundaries, our method effectively handles the non-manifold film geometry, as shown in Figure 6 (Middle) and Figure 14.

To summarize, the inter-liquid gap is discretized into single-layered air cells, with cut-cell meshes of liquid volumes serving as their top and bottom boundaries. The lateral boundaries of the air cells are defined as half faces along the periphery of the top and bottom boundaries, where the tangential velocity within the film is defined.

3.2 | Discrete differential operators

Next, we will build discrete differential operators for the liquid volumes, air film, and their interfaces. We provide a comprehensive explanation of gradient operators as an example and visualize them in Figure 5. The divergence and Laplacian operators can be derived in a similar manner. Additionally, we summarize these density-weighted gradient operators within Table 1.

Gradient operator in liquid

In a liquid domain, the gradient is defined as $\nabla p = (p_{1,l} - p_{1,m})/d_{lm}$ between two liquid cell l, m, with the pressure samples $p_{1,l}$, $p_{1,m}$ on the iso-surfaces of cells and $d_{lm} = |x_l - x_m|$, as depicted in Figure 5 (Left). On the ambient air interface Γ_{13}, we modify the gradient equation by placing the interfacial pressure sample $p_{1,m}$ at the center of the cut face and setting it equal to the boundary condition p_{atm}. We use $\mathbf{S}_1 \hat{\mathbf{G}}_1 \mathbf{p}_1$ to represent the matrix form of the pressure gradient acceleration $\nabla p/\rho$ in the liquid domain. $\mathbf{p}_1$ stands for the liquid pressure vector. $\hat{\mathbf{G}}_1$ is a difference matrix with elements 1 and -1, denoting the pressure difference across the grid faces and cut faces of Γ_{13}. $\mathbf{S}_1$ is a diagonal matrix with elements $1/(\rho_1 d_{lm})$, which can be regarded as the inverse of the area density in the control volume of the face between $p_{1,l}$ and $p_{1,m}$.

Gradient operator in air film

The tangent pressure gradient in the air film is defined on the half faces between adjacent air pressure degrees of freedom. As shown in Figure 5 (Right), we sample the pressure $p_{2,l}$, $p_{2,m}$ at the center of air cells x_l, x_m and discretize the gradient $\nabla p = (p_{2,l} - p_{2,m})/(|x_l - x_m|)$ on the half faces. On the ambient air interface Γ_{23}, we place the pressure sample of the ambient air $p_{2,m}$ on the half face. And the distance between two samples is defined as $|(x_l - x_r) \cdot e_t|$, where x_r is the position of the rim (rim vertex in 2D, midpoint of rim edge in 3D), e_t is the tangent unit vector at x_r parallel to $u_{t\uparrow}$ or $u_{t\downarrow}$. We use $\mathbf{p}_2$ to denote the air film pressure vector and $\hat{\mathbf{G}}_2$ to denote the tangent pressure difference operator on the half faces.

Gradient operator on air-liquid interface

Across the interface Γ_{12} between the liquid volumes and the air film, the acceleration caused by pressure gradient $\nabla p / \rho$ is continuous. Disregarding the jump condition, the acceleration on a cut face between the liquid sample $p_{1,l}$ and the air film sample $p_{2,m}$ is discretized as $\nabla p / \rho = (p_{1,l} - p_{2,m})/(\rho_1 d_l + \rho_2 h_{lm}/2)$, where d_l is the distance from the liquid pressure sample to the cut face, $h_{lm}/2$ is the half thickness evaluated at the cut face, as shown in Figure 5 (Middle). The acceleration across Γ_{12} is given as $\mathbf{S}_\Gamma \hat{\mathbf{G}}_\Gamma (\mathbf{p}_1^T, \mathbf{p}_2^T)^T$, where $\mathbf{S}_\Gamma$ is a diagonal matrix with elements $1/(\rho_1 d_l + \rho_2 h_{lm}/2)$ describing the inverse of face density in the control volume of the cut faces. $\hat{\mathbf{G}}_\Gamma = (\hat{\mathbf{G}}_{\Gamma,1}, \hat{\mathbf{G}}_{\Gamma,2})$ is the difference matrix across the interface. Each row of $\hat{\mathbf{G}}_{\Gamma,1}$ picks out the adjacent liquid pressure sample of the cut face and assigns 1. In contrast, each row in $\hat{\mathbf{G}}_{\Gamma,2}$ assigns -1 for the adjacent air film sample. Thus, $\hat{\mathbf{G}}_\Gamma (\mathbf{p}_1^T, \mathbf{p}_2^T)^T$ returns a vector where the entries are pressure differences between the liquid and the air film on the cut faces of Γ_{12}.

TABLE 1 Discretized gradient operators on between different cells.

| Cell type l	Cell type m	$\nabla p/\rho$
Liquid	Liquid	$\frac{p_{1,l} - p_{1,l}}{\rho_1 |x_l - x_m|}$
Liquid	Ambient air	$\frac{p_{1,l} - p_{atm}}{\rho_1 |x_l - x_\theta|}$
Air	Air	$\frac{p_{2,l} - p_{2,m}}{\rho_2 |x_l - x_m|}$
Air	Ambient air	$\frac{p_{2,l} - p_{atm}}{\rho_2 |(x_l - x_r) \cdot e_t|}$
Liquid	Air	$\frac{p_{1,l} - p_{2,m}}{(\rho_1 d_l + \rho_2 h_{lm})/2}$

4 | COUPLING SYSTEM

Building upon the sub-cell discretization and its discrete differential operators, we propose a two-way coupling method for solving the pressure monolithically across both the liquid volumes and the air gap. This method couples the inviscid liquids and the lubricated air film through their cut-cell interface, which enforces the continuous velocity constraint naturally. We will now introduce the pressure projection equation for liquids and air film and derive their coupling system.

Liquid domain

The pressure projection equation for the liquid is discretized on the liquid cells, which gives

$$\Delta t \sum_{\mathcal{F}_g} \frac{A_g}{\rho_1} \nabla p_1 + \Delta t \sum_{\mathcal{F}_n} \frac{A_n}{\rho_1} \frac{\partial p_1}{\partial \xi_n} = \sum_{\mathcal{F}_g} A_g u_g + \sum_{\mathcal{F}_n} A_n u_n \tag{7}$$
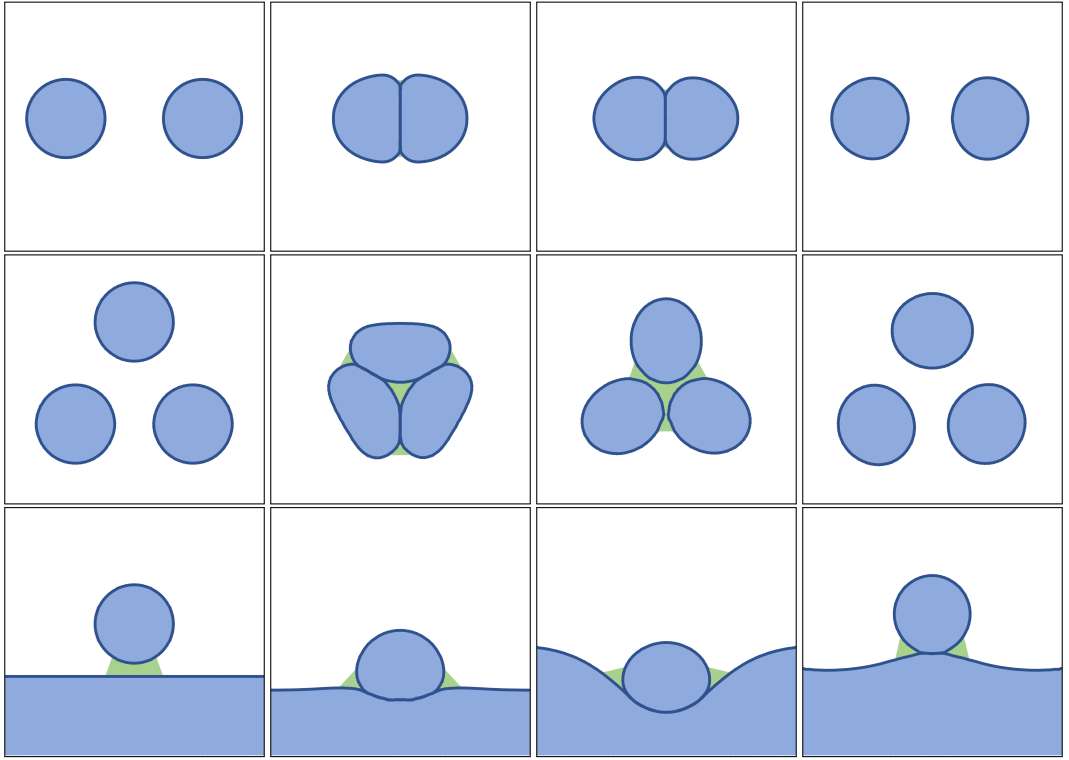
FIGURE 6 *Time evolution of 2D scenarios. Top:* binary droplet collision. *Middle:* trinary droplet collision. *Bottom:* bouncing droplet. Liquid volumes (blue) are visualized and air films (green) are depicted in the latter two examples.

where $\mathcal{F}_g$ is the set of the grid faces, and the cut faces on the ambient air boundary Γ_{13}, $\mathcal{F}_n$ is the set of the cut faces on the boundary Γ_{12}. u_g is the velocity sampled on the faces $\mathcal{F}_g$. u_n is the normal velocity on the center of the cut faces $\mathcal{F}_n$. A_g and A_n denote the area of the corresponding faces.

Using the differential operator in Section 3.2, we rewrite Equation (7) in a matrix form as

$$\Delta t \hat{\mathbf{G}}_1^T \mathbf{A}_1 \mathbf{S}_1 \hat{\mathbf{G}}_1 \mathbf{p}_1 + \Delta t \hat{\mathbf{G}}_{\Gamma,1}^T \mathbf{A}_\Gamma \mathbf{S}_\Gamma (\hat{\mathbf{G}}_{\Gamma,1} \mathbf{p}_1 + \hat{\mathbf{G}}_{\Gamma,2} \mathbf{p}_2)$$
$$= \hat{\mathbf{G}}_1^T \mathbf{A}_1 \mathbf{u}_1 + \hat{\mathbf{G}}_{\Gamma,1}^T \mathbf{A}_\Gamma \mathbf{u}_\Gamma \tag{8}$$

where $\hat{\mathbf{G}}_1$ is the pressure difference operator on the grid faces in Ω_1 and the cut faces on Γ_{13}. $\hat{\mathbf{G}}_{\Gamma,1} \mathbf{p}_1 + \hat{\mathbf{G}}_{\Gamma,2} \mathbf{p}_2$ is the pressure difference across the liquid-air-film interface Γ_{12}. $\mathbf{A}_1$ and $\mathbf{A}_\Gamma$ are the diagonal area matrices for the liquid faces in $\Omega_1 \cup \Gamma_{13}$ and the cut faces on Γ_{12}, respectively. $\mathbf{u}_1$ is the velocity vector for the liquid faces in $\Omega_1 \cup \Gamma_{13}$ and $\mathbf{u}_\Gamma$ is the velocity vector for the cut faces on Γ_{12}.

Air film

Discretizing Equation (5) on a irregular air cell gives

$$\sum_{\mathcal{F}_t} \frac{h_t^2 A_t}{12\mu_2} \frac{\partial p_2}{\partial \xi_t} + \Delta t \sum_{\mathcal{F}_n} \frac{A_n}{\rho_2} \frac{\partial p_2}{\partial \xi_n} = \sum_{\mathcal{F}_t} A_t u_t + \sum_{\mathcal{F}_n} A_n u_n \tag{9}$$

where $\mathcal{F}_t$ is the set of the lateral half faces of the air cell, $\mathcal{F}_n$ is the set of the cut faces on its normal boundary in Γ_{12}, u_t is the boundary tangent velocity on the half faces which represents both $u_{t\uparrow}$ and $u_{t\downarrow}$, u_n is the normal velocity on the center of the cut faces, h_t is the thickness evaluated at the rim of the half face, A_t and A_n denote the area of the half faces and the cut faces.

The matrix form of Equation (9) for the air film becomes

$$\begin{aligned}
&\frac{1}{12\mu_2} \hat{\mathbf{G}}_2^T \mathbf{V}_2 \hat{\mathbf{G}}_2 \mathbf{p}_2 + \Delta t \hat{\mathbf{G}}_{\Gamma,2}^T \mathbf{A}_\Gamma \mathbf{S}_\Gamma (\hat{\mathbf{G}}_{\Gamma,1} \mathbf{p}_1 + \hat{\mathbf{G}}_{\Gamma,2} \mathbf{p}_2) \\
&= \hat{\mathbf{G}}_2^T \mathbf{A}_2 \mathbf{u}_2 + \hat{\mathbf{G}}_{\Gamma,2}^T \mathbf{A}_\Gamma \mathbf{u}_\Gamma
\end{aligned} \tag{10}$$

where $\hat{\mathbf{G}}_2$ is the tangent difference operator mapping the pressure difference onto the half faces, $\mathbf{V}_2$ is a diagonal matrix denoting $\left(h^2 A\right)/d$ with the thickness h, half face area A and sample distance d evaluated on the half faces between two air cells. $\mathbf{u}_2$ is the tangent velocity vector containing $u_{t\uparrow}$ and $u_{t\downarrow}$ on the half faces.

Fully-coupled system

Combining Equation (8) and Equation (10) yields the fully-coupled system.

$$\begin{aligned}
&\begin{bmatrix}
\Delta t \hat{\mathbf{G}}_1^T \mathbf{A}_1 \mathbf{S}_1 \hat{\mathbf{G}}_1 + \Delta t \hat{\mathbf{G}}_{\Gamma,1}^T \mathbf{A}_\Gamma \mathbf{S}_\Gamma \hat{\mathbf{G}}_{\Gamma,1} & \Delta t \hat{\mathbf{G}}_{\Gamma,1}^T \mathbf{A}_\Gamma \mathbf{S}_\Gamma \hat{\mathbf{G}}_{\Gamma,2} \\
\Delta t \hat{\mathbf{G}}_{\Gamma,2}^T \mathbf{A}_\Gamma \mathbf{S}_\Gamma \hat{\mathbf{G}}_{\Gamma,1} & \Delta t \hat{\mathbf{G}}_{\Gamma,2}^T \mathbf{A}_\Gamma \mathbf{S}_\Gamma \hat{\mathbf{G}}_{\Gamma,2} + \frac{1}{12\mu_2} \hat{\mathbf{G}}_2^T \mathbf{V}_2 \hat{\mathbf{G}}_2
\end{bmatrix} \cdot \begin{bmatrix} \mathbf{p}_1 \\ \mathbf{p}_2 \end{bmatrix} \\
&= \begin{bmatrix}
\hat{\mathbf{G}}_1^T \mathbf{A}_1 \mathbf{u}_1 + \hat{\mathbf{G}}_{\Gamma,1}^T \mathbf{A}_\Gamma \mathbf{u}_\Gamma \\
\hat{\mathbf{G}}_2^T \mathbf{A}_2 \mathbf{u}_2 + \hat{\mathbf{G}}_{\Gamma,2}^T \mathbf{A}_\Gamma \mathbf{u}_\Gamma
\end{bmatrix}
\end{aligned} \tag{11}$$

This system is symmetric and positive definite and is amenable to high-performance algebraic multi-grid solvers. To ensure the volume conservation of each fluid region during the simulation, we adopt the divergence control method proposed in [78].

5 | TIME INTEGRATION

We summarize our temporal evolution scheme in Algorithm 1. At the beginning of each frame, the node-based level sets and the velocity fields are advected using the MacCormack method (Section 5.1). After the advection, the gap geometry is fixed (Section 5.2). Then, we generate the cut cells of the liquid volumes using the marching cube method and discretize the air film into single-layered irregular cells (Section 5.3). Body forces, including gravity, are applied explicitly, and the surface tension is solved implicitly on fluid regions (Section 5.4). Finally, our method couples the pressure degrees of freedom in the liquids and the air film through their interfaces and solves the two-way coupling system (Section 4).

5.1 | Advection

As discussed in [13], the inertia of the air film can be considered negligible in simulation when the gaseous kinetic energy is much smaller compared to the Laplace pressure, which holds for all small-scale scenarios in our paper. Therefore, in this step, we only advect the liquid volumes. We perform the MacCormack method [79] to update the node-based level set and velocity field of each liquid volume according to its extrapolated velocity field. Given that the level set values, especially those distant from the interfaces, deviate from the expected values after the advection, we reinitialize level sets by employing the fast-marching algorithm.

5.2 | Fixing gap geometry

Due to the significant difference in scale of the system, even trivial numerical errors from advection and interpolation can lead to negative air film thickness. We address the issue by performing Jacobi-style iterations of local correction on the cut vertices with negative thickness. Given the cut vertex x on the grid edge e and the liquid interface $\partial\Omega_{1,j}$, if it is found to be inside another liquid volume $\Omega_{1,k}$ ($\phi_k(x) < 0$), the local correction update the level set value on both nodes of e by $\phi_j + = (|\phi_k(x)| + h_e)/2$. h_e is the minimal thickness threshold determined empirically.

5.3 | Updating cell geometry

In each time step, we update the cell geometry on both liquid volumes and the air film. For the liquid volumes, we regenerate the cut-cell mesh and reposition the pressure samples on the iso-surface. Based on the interface mesh of liquids, irregular air cells are constructed.

Cut cells in liquid volumes

For each liquid volume, we perform the marching cube algorithm on its node-based level set to obtain its cut-cell mesh. We then update the pressure samples on the cut cells, following a method proposed in [70], to achieve second-order accuracy and maintain discretization orthogonality on the cut cells.

Irregular cells in the air film

The process of the air cell construction is illustrated in Figure 7. Given a pair of liquid volumes $\{\Omega_{1,j}, \Omega_{1,k}\}$, the air film is defined as the region where $h < h_{max}$. We employ graph theory to establish a many-to-many mapping between cut faces from two liquid volumes, and then group the neighboring cut faces to construct single-layered air cells.

We first define an iso-contour surface at $\phi_j - \phi_k = 0$, which is also the ridge of $\min(\phi_j, \phi_k)$. A set of ridge vertices $\mathcal{V}$ are sampled at the intersections of this ridge surface and the grid edges. Then, an auxiliary graph is initialized with these ridge vertices $\mathcal{V}$ and the cut faces $\mathcal{F}_j \cup \mathcal{F}_k$ as the graph nodes. Note that only the cut faces with local thickness

---

Algorithm 1 Temporal evolution for a single timestep

1: Advect liquid level sets and velocity fields (Section 5.1)
2: Fix gap geometry to avoid penetration (Section 5.2)
3: Update cell geometry for liquid and air (Section 5.3)
4: Apply body forces
5: Solve implicit surface tension (Section 5.4)
6: Solve the two-way coupling system (Section 4)
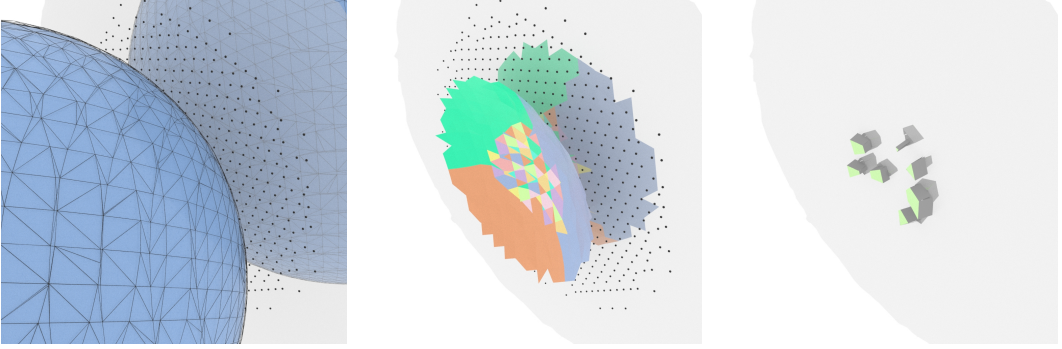
FIGURE 7 *Illustration of irregular cell construction for the air film. Left:* The surface mesh of two liquid volumes Ω_j, Ω_k (blue surface with wireframes) is visualized. First, the ridge vertices (black dots) are sampled at the intersections of grid edges and the ridge surface (grey surface) where $\phi_j - \phi_k = 0$. *Middle:* Next, We construct a graph with cut faces and ridge vertices as the graph vertices and initialize its edges based on the closest neighbor search. We then divide the cut faces into multiple groups (colored mesh) based on the connectivity of the graph. *Right:* Finally, the air cells (green cells) are constructed based on the groups of cut faces. For clarity purposes, only a subset of air cells is visualized in this figure. The top and bottom boundaries of air cells are defined by the cut faces (green faces). The lateral cell boundaries are defined by the half faces (grey faces) positioned along the edge of the cut faces.

$h < h_{max}$ are involved. We search for the closest cut faces for each ridge vertex and establish edges between each ridge vertex and its closest cut faces in $\mathcal{F}_j$ and $\mathcal{F}_k$, as well as between each cut face and its closest ridge vertex. For each connected subgraph, we group the cut faces within the same subgraph and construct irregular air cells with these cut faces serving as their boundary meshes on air-fluid interfaces. The lateral cell boundary of a newly generated air cell is discretized as the half faces orthogonal to the rims of the boundary meshes as described in Section 3.1. The normal and tangential velocities on its boundary are interpolated from the velocity fields of corresponding liquid volumes and projected onto the corresponding directions. To determine the center of the air cell, we compute the average position of its vertices and project it onto the ridge surface.

5.4 | Semi-implicit surface tension

Instead of treating surface tension as the interface pressure jump in pressure projection, we solve the semi-implicit surface tension [46] on a narrow band around the interface weighted by a Dirac function for each fluid region independently. The faces within $\phi(\boldsymbol{x}) < \Delta x_\sigma$ are included in the equation:

$$(1 - \frac{1}{\rho}\sigma\Delta t^2\nabla^2)\boldsymbol{u}^* = \boldsymbol{u} + \frac{1}{\rho}\delta(\phi)\sigma\kappa\vec{n}\Delta t \tag{12}$$

where the Dirac function is

$$\delta(\phi) = \frac{1 + \cos\frac{\pi\phi}{\Delta x_\delta}}{2\Delta x_\delta}, \text{ if } \phi \in [-\Delta x_\sigma, \Delta x_\sigma] \tag{13}$$
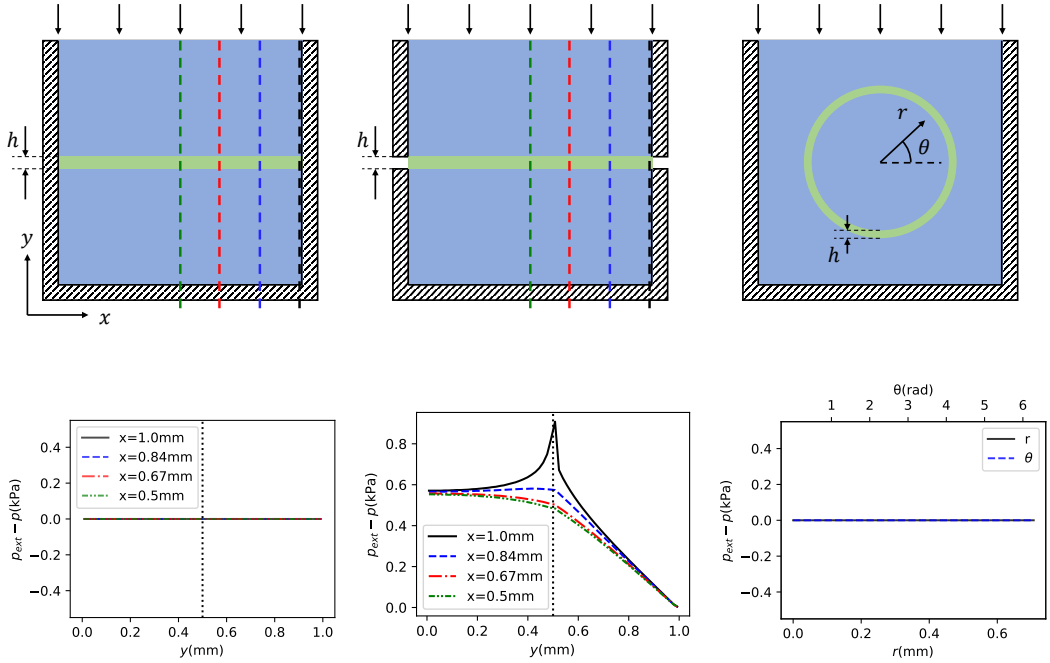
FIGURE 8 *Numerical validation of pressure transmission across the air film.* A series of scenes are set up, where an air film is confined in a piston filled with liquids, and a constant pressure $p_{ext} = 1000$ kPa is applied on the upper boundary. The illustration of the scene and the plot of the pressure loss $p_{ext} - p$ are shown. *Left:* A planar air film trapped between two liquid regions in a piston. The pressure losses evaluated at $x = 1.0, 0.84, 0.67, 0.5$ mm show that the external pressure is transmitted throughout the whole domain and results in an identical pressure field. *Middle:* The same air film is trapped with its left and right boundaries connected to the ambient air. The same pressure samples are evaluated, indicating that the thin film is capable of transmitting the majority of pressure even close to the ambient air boundary. *Right:* An annular air film is trapped in the liquid, with a constant pressure applied on the upper boundary. The radial pressure loss distribution and the pressure loss along the annular film are plotted, which match the boundary pressure condition.

with the band width $\Delta x_\delta = 3\Delta x$. The zero-velocity Dirichlet boundary condition is enforced. We then discretize Equation (12) as a symmetric linear system with $\boldsymbol{u}^*$ as unknown values, and employ the algebraic multi-grid solvers for its solution.

6 | RESULTS

6.1 | Numerical validations in 2D

To validate our coupled pressure projection, we set up a set of two-dimensional numerical tests.
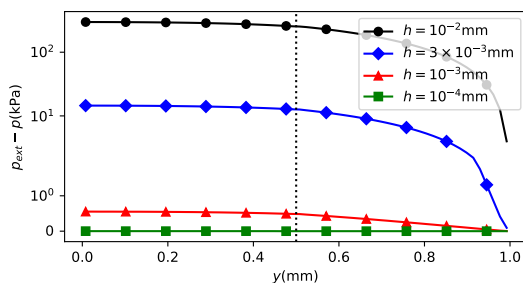
FIGURE 9 *The pressure transmission in Figure 8 (Middle) with different air film thickness h.* The pressure loss along the vertical lines at $x = 0.5$ mm is plotted.

### 6.1.1 | Air film pressure transmission

In this two-dimensional test, a thin air film is trapped between two liquid volumes in a solid piston with zero gravity, as illustrated in Figure 8 (Left). A constant pressure is applied to the upper boundary of the liquid, resulting in a high pressure inside the piston. Due to the incompressibility, the analytical solution should be a constant pressure field throughout the entire domain. The simulation is conducted in a 1 mm×1 mm domain divided into a 64×64 grid. The air film locates at $y = 0.5$ mm with the thickness $h = 1 \times 10^{-3}$ mm. The density of the liquid and the air are $\rho_1 = 1000\,\text{kg/m}^3$, $\rho_2 = 1\,\text{kg/m}^3$. A Dirichlet pressure boundary condition of $p_{ext} = 1000\,\text{Pa}$ is applied to the upper domain boundary and Neumann pressure boundary conditions are applied to all solid boundaries. The resulting pressure on vertical lines $x = 1.0, 0.84, 0.67, 0.5$ mm are identical to the constant external pressure, which is consistent with the analytical solution.

6.1.2 | Air film pressure transmission with the open boundary

We further assess the pressure transmission through the planar air film with its left and right boundaries connected to the ambient air, similar to the liquid-air-film system in real-world scenes. The configurations are identical to the test in Section 6.1.1, with the exception of the zero pressure boundary condition being applied at the left and right boundaries of the air film.

We analyze the pressure loss distribution along four vertical lines at $x = 0.0, 0.17, 0.34, 0.5$ mm. The results in Figure 8 (Middle) show that although the pressure slightly decreases as it moves down, about 99.99% of the pressure is successfully transmitted to the lower liquid volume. Therefore, when two liquids collide, the thin air film acts like an air cushion even if it is connected to the ambient air, and is able to transmit the pressure between them to avoid coalescence.

We also examine the effect of air film thickness on pressure transmission. Figure 9 shows the pressure loss sampled along the vertical line at $x = 0.5$ mm for various thicknesses $h = 10^{-2}, 3 \times 10^{-2}, 10^{-3}, 10^{-4}$ mm. The results support the intuitive assumption that as the air film gets thinner, the pressure transmission loss across the air film decreases.
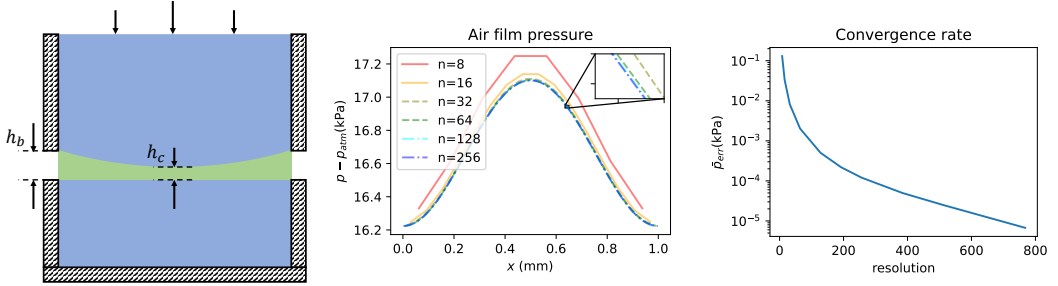
FIGURE 10 *Convergence validation of pressure in the air film with varying thickness.* We investigate the convergence behavior of our method in a scene with a 2D thin air film of varying thickness. *Left:* The scene overview depicts varying pressure applied to the top boundary, with a thin air film (green) of thickness ranging from h_c to h_b trapped between two liquid volumes (blue). *Middle:* The resulting pressure distribution within the air film at different resolutions. *Right:* The convergence rate is depicted, showing a decrease in average pressure error as resolution increases.

6.1.3 | Annular air film pressure transmission

In Figure 8 (Right), we demonstrate the ability of our solver to handle a curved air film. An annular air film is trapped in the liquids, with the same boundary conditions in Section 6.1.1. The film is centered in the domain with the thickness $h = 1 \times 10^{-3}$ mm and radius 0.25 mm. the constant pressure is obtained throughout the liquid volume and the air film, in agreement with the analytic solution.

6.1.4 | Air film pressure at different resolutions

To further validate the convergence behavior of our method, we examine a scenario involving a thin film trapped between two liquid volumes, as illustrated in Figure 10 (Left). An external pressure is applied at the upper boundary, following the function $p_{ext}(x) = 100 \times (0.5^2 - (x - 0.5)^2)$ kPa. We define the film thickness as $h(x) = h_c + R - \sqrt{R^2 - (x - 0.5)^2}$, mimicking the thin film trapped between a spherical droplet and a planar liquid tank. Specifically, we set $h_c = 10^{-5}$ mm and $R = 12500$ mm, ensuring that the thickness ranges within $[h_c, h_b]$ ($h_b = 2 \times 10^{-5}$ mm). We solve this static scene at various resolutions and plot the resulting pressure distribution within the air film in Figure 10 (Middle), showing convergence towards a consistent curve. Additionally, we compute the average absolute error by comparing the air film pressure with that at resolution 1024×1024, as depicted in Figure 10 (Right), demonstrating convergence as the resolution increases.

6.1.5 | Droplet impact with different film height thresholds

We simulate a two-dimensional droplet impacting a liquid bath to evaluate the effect of h_{max}, which is used as a numerical threshold to distinguish the air film from the ambient air. The simulation is initialized in a 1 mm×1 mm domain with $\Delta x = 1/64$ mm, where the droplet is placed at $(0.5, 0.5)$ with radius $r = 0.15$ mm and the bath is initialized with the depth $h_B = 0.3$ mm. The surface tension of the liquid is $\sigma = 1.66$ mN/m and its density is $\rho_1 = 1000$ kg/m³. The air density is $\rho_2 = 1$ kg/m³ and its viscosity is $\mu_2 = 18.6$ uPas The simulation is run with the gravity $g = -9.8$ m/s² and the time step $\Delta t = 5 \times 10^{-4}$ s.
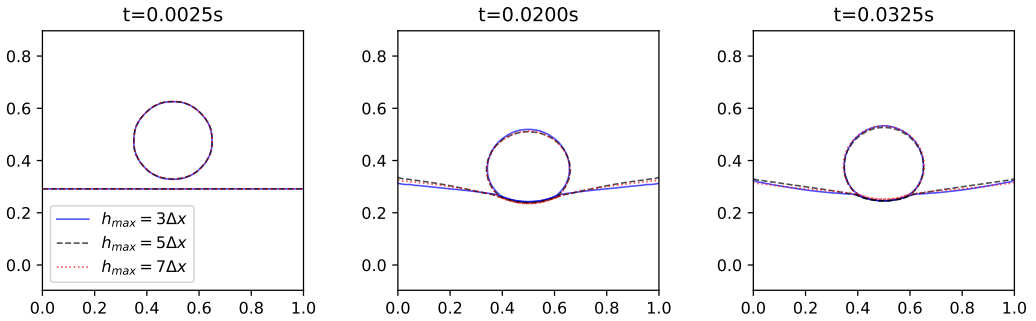
FIGURE 11 A 2D droplet falls on the liquid bath with different air film height thresholds $h_{max} = 3\Delta x, 5\Delta x, 7\Delta x$

Figure 11 shows the results with $h_{max} = 3\Delta x$, $5\Delta x$ and $7\Delta x$, which validates that the thickness threshold won't affect the overall motion of the simulation. We also found that a small threshold $h_{max} = \Delta x$ would lead to instability due to the potential incorrect geometry in air film initialization, while a too-large threshold would introduce additional overhead on thick air film where the resulting pressure has a negligible effect on the liquids. Therefore, we use $h_{max} = 5\Delta x$ for the remaining simulations in this work.

6.1.6 | Binary collision at different resolutions

We also conduct simulations of two-dimensional binary droplet collisions to assess convergence under varying resolutions. The scene is set within a domain of 1 mm×1 mm, where two droplets with a radius of $r = 0.15$ mm are initialized at $(0.5 \pm 0.27, 0.5)$ with opposite initial velocities of 60 mm/s.

Figure 12 depicts the results obtained with resolutions 64×64, 128×128, 192×192, 256×256, 320×320. The absolute error is shown in Figure 12 (Bottom left). The y-axis radii of the droplets (r_0, r_1) are evaluated as half the width of the droplets. As the resolution increases, the simulations tend to converge toward consistent results, with a decreasing convergence rate.

6.1.7 | Binary droplet collision, trinary droplet collision, bouncing droplet in 2D

In Figure 6 (Top), we simulate the two-dimensional binary collision by emitting two identical spherical droplets with opposite initial velocities. During the head-on collision, the air film exerts resistance to droplet coalescence, resulting in the droplets bouncing apart. We also simulate the trinary collision in Figure 6 (Middle), which demonstrates the ability of our method to handle non-manifold joints in thin films.

We further simulate the two-dimensional bouncing droplet. The bath oscillates vertically with the period 0.02 s and the peak acceleration 9.8 m/s². As shown in Figure 6 (Bottom), the droplet is able to bounce over the bath periodically and stably for a long time, which indicates the stability of our algorithm.
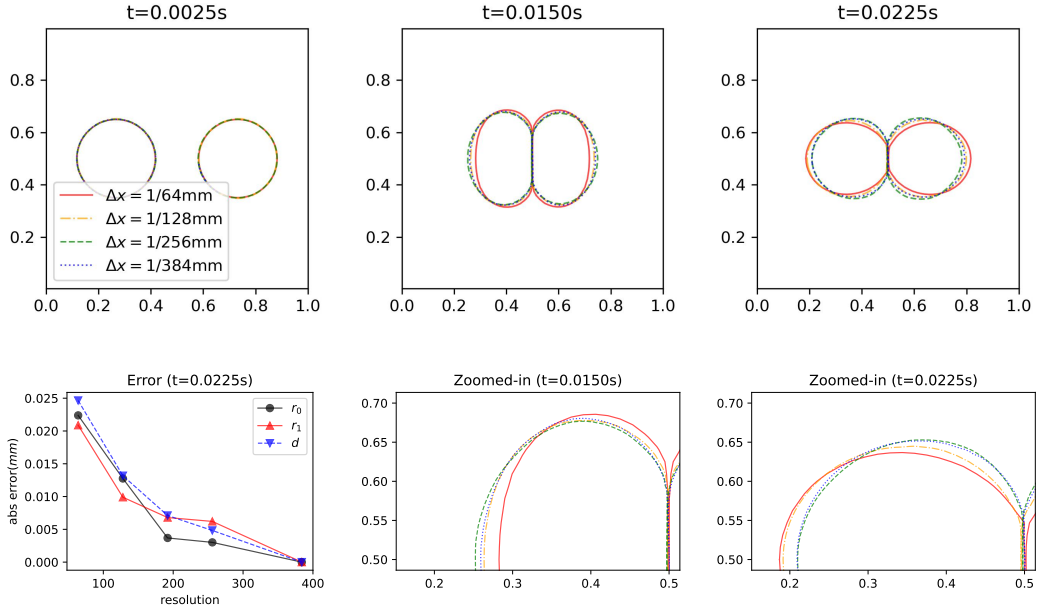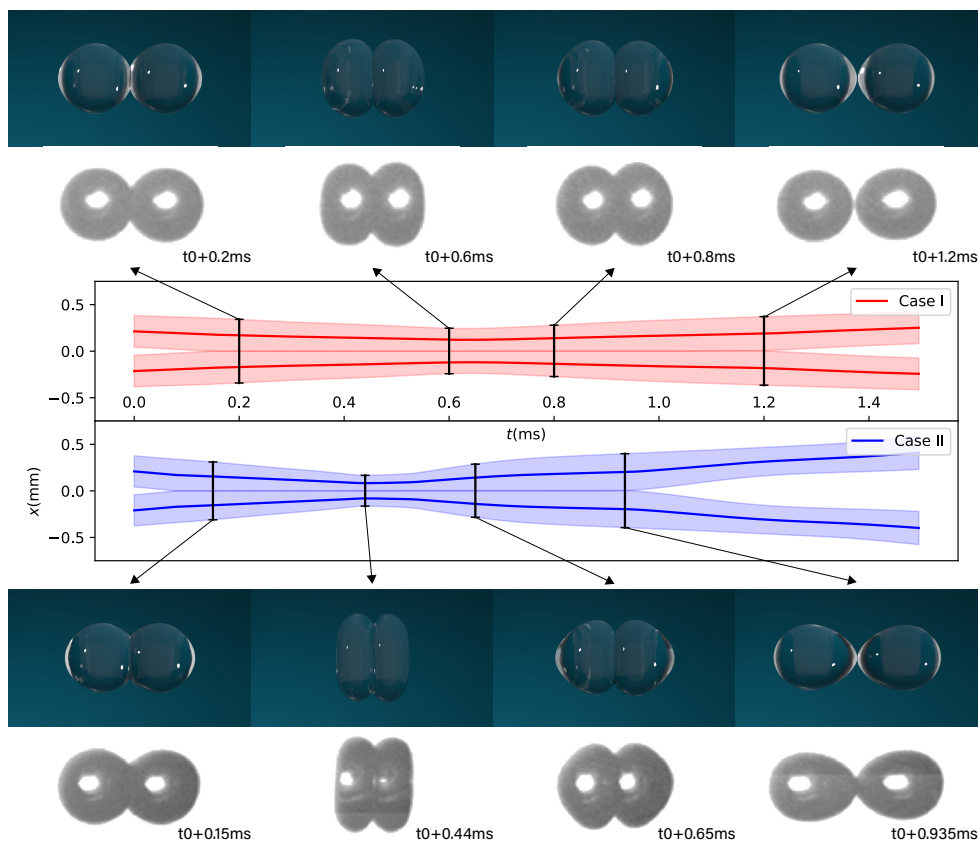
FIGURE 12 *2D binary droplet collision at various resolutions. Top:* Simulation results with resolutions of 64×64, 128×128, 192×192, 256×256, 320×320. *Bottom left:* Absolute error of two droplet radii (r_0, r_1) in y-axis and their centroid distance (d) evaluated at $t = 0.0255s$. *Bottom middle and right:* Zoomed-in results of the upper part of the left droplet at $t = 0.0150, 0.0255s$.

6.2 | Binary droplet collision

We follow the experimental study [1] to set up the experiments of head-on binary tetradecane droplet collisions. Two tetradecane droplets are initialized in 1 atm ambient air, with the density $\rho_1 = 762 \, \text{kg/m}^3$ and the surface tension coefficient $\sigma = 26.56 \, \text{mN/m}$. The density of the air film trapped in the gap is $\rho_2 = 1 \, \text{kg/m}^3$, and the viscosity is $\mu_2 = 18.6 \, \text{uPas}$. The simulation is conducted with the time step $\Delta t = 5 \times 10^{-6}$ s on a $256 \times 128 \times 128$ background grid with $\Delta x = 1/128$ mm.

In Case I, the droplets with the radius $R = 0.1706 \, \text{mm}$ are placed along the x-axis with the distance between the droplet centers $D_0 = 2.5R$ and emitted in opposite directions with an initial velocity $V_0 = 0.243 \, \text{m/s}$. In Case II, the collision occurs between two droplets with the radius $R = 0.1676 \, \text{mm}$ and the initial velocity $V_0 = 0.496 \, \text{m/s}$, resulting in larger deformation. The Weber number is We= 2.27 for Case I and is We= 9.33 for Case II.

The time series of the droplets are visualized in Figure 13 with our simulation results and the photographs obtained from the experiments in [1]. Specifically, four representative frames are compared, including the initial contact, maximum deformation, rebound, and detachment. Our results, which use the same configurations, agree well with the experimental results in terms of contact time and droplet deformation.
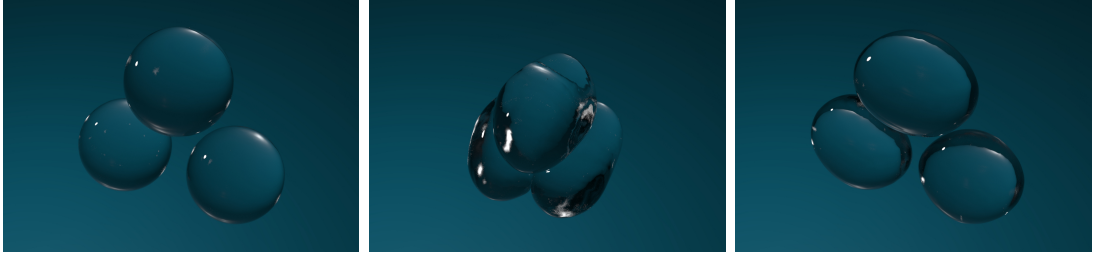
FIGURE 13 *Time evolution of the binary droplet collision for Case I and II. Top and Bottom:* Representative frames of the rendered images from our simulation and the experimental snapshots from [1]. *Middle:* The evolution of the *x*-axis positions of two droplets. The regions filled by the light color are the *x*-axis bounding box of two droplets. Solid lines denote the *x*-axis center position of two droplets.

6.3 | Trinary droplet collision

We further conduct the experiment where three tetradecane droplets collide and rebound. We emit three tetradecane droplets with radius $R = 0.1706$ mm in 1 atm ambient air, with the density $\rho_1 = 762$ kg/m³, the surface tension coefficient $\sigma = 26.56$ mN/m and the initial velocity $V_0 = 0.5 m/s$. The density of the air film is $\rho_2 = 1$ kg/m³, and the viscosity is $\mu_2 = 18.6$ uPas. We discretize the domain on a $128 \times 128 \times 128$ background grid with $\Delta x = 1/128$ mm and conduct the simulation with the time step $\Delta t = 5 \times 10^{-6}$ s.

The simulation result is depicted in Figure 14, showcasing the collision of three identical droplets followed by their rebound. Note that the air film exhibits a non-manifold joint, demonstrating the ability of our method to handle complex non-manifold geometry.

FIGURE 14 *Time evolution of the trinary droplet collision.* Three droplets collide, form a non-manifold gap between them and subsequently rebound.
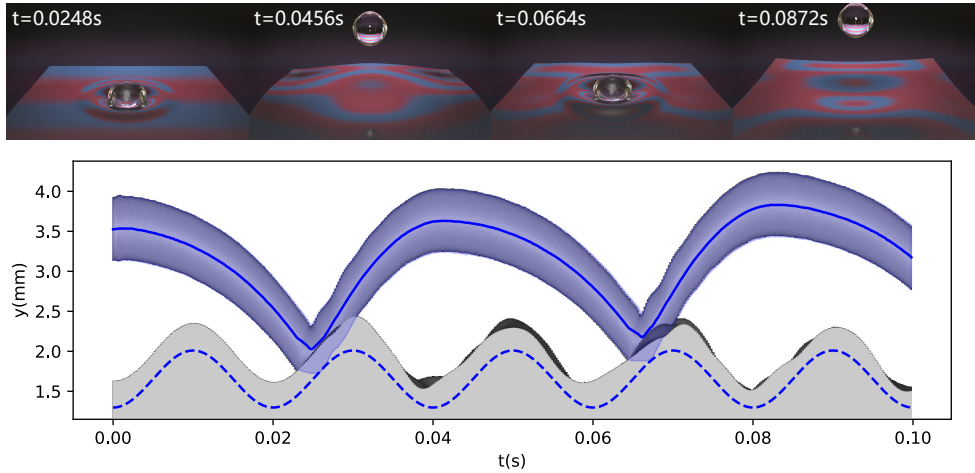

FIGURE 15 *Time evolution of a droplet bouncing on a vibrating bath in* $(2, 1)$ *mode.* *Top:* Rendered images of four representative frames. *Bottom:* Temporal evolution of the scene. The solid line denotes the movement of the droplet center, and the dashed line denotes the bath movement. The background image is generated by stitching the successive simulation frames, where a cropped vertical section represents each frame through the droplet center.

6.4 | Bouncing droplet on a vibrating bath

We reproduce the bouncing droplet reported in [2] where a silicon oil droplet is released on an oscillating silicon oil bath. The container is vibrating vertically with the acceleration $a_B = \gamma sin(2\pi f t)$, where f is the frequency, and γ is the peak acceleration. As discussed in [2], different periodic bouncing modes (m, n) of the droplets are observed. In a (m, n) bouncing mode [27, 2], the droplet bounces steadily with the period equal to m/n times of the bath vibration period. Intuitively, it means the droplet contacts the bath n times within m bath oscillating periods.

In our simulation, we release a silicon oil droplet with the undeformed radius $R_0 = 0.39mm$, with surface tension $\sigma = 20.6$ mN/m and density $\rho_1 = 949$ kg/m^3. The bath is shaken vertically with $f = 50$ Hz and $\gamma = 35.28$ m/s^2. The non-dimensional bath acceleration is $\Gamma = \gamma/g = 3.6$. The simulation is conducted in a $5 \times 5 \times 5$ mm domain divided into 256^3 grid cells, with the time step $\Delta t = 2 \times 10^{-4}$ s.

In Figure 15, the vertical sections through the droplet center are rendered and joined together by frame order.
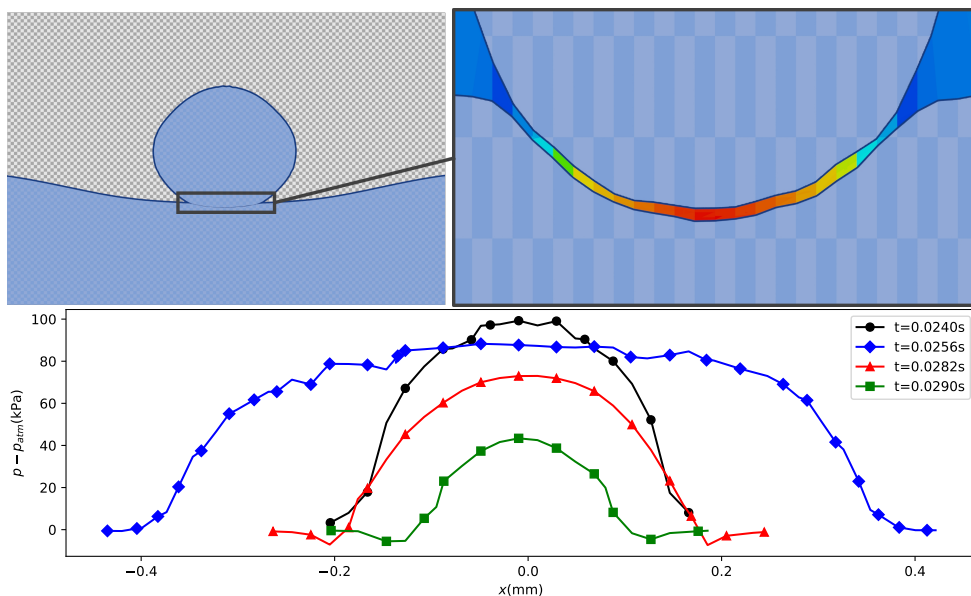
FIGURE 16 *The air film pressure distribution of the bouncing droplet. Top left:* The section view of the domain across the droplet center at $t = 0.0282s$. The background grid is colored with the checkerboard pattern to visualize the cells. *Top right:* A zoom-in section view of the pressure distribution in the air film. The coordinate system is stretched vertically to enhance visualization. *Bottom:* The pressure distribution in the air film during the first impact. The pressures are sampled on the same section across the droplet center.

The droplet trajectory and the sinusoidal motion of the liquid surface are plotted on the spatiotemporal image. Our simulation reproduces the $(2, 1)$ bouncing mode reported in [2], where the droplet bounces once every two vibration periods of the bath. Whenever the droplet touches the bath, the bath is always in its upward phase of the period and propels the droplet back.

The pressure distribution in the air film on a cross-section across the droplet center is visualized in Figure 16. At the beginning of the impact, a narrow pressure peak in the air film arises due to the large relative velocity between the two liquids. As the droplet deforms, the pressure is distributed over a larger area of the air film. As its upward velocity is restored, the air film pressure declines until the droplet separates from the bath.

6.5 | Promenading pairs of droplets

As reported in the previous work [38], when two identical droplets bounce on an oscillating liquid bath, they exhibit a behavior known as the promenading mode. In this mode, the droplets interact with each other through the wave field and vibrate laterally along the line across their centers. In our simulation, the silicon oil with the density $\rho_1 = 949\,\text{kg/m}^3$ and the surface tension $\sigma = 20.6\,\text{mN/m}$ is used for both droplets and the liquid bath. The radius of the undeformed droplets is $R = 0.8\,\text{mm}$, and the bath is vibrated vertically with $f = 80\,\text{Hz}$, $\Gamma = 0.45$ and $\gamma = 4.41\,\text{m/s}^2$. The initial distance between the droplet centers is $D_0 = 4\,\text{mm}$ in Case I and $D_0 = 2.4\,\text{mm}$ in Case II. To reduce the accumulated error caused by long-term simulation, we simulate the two phases (approaching and leaving each other) of the promenading mode separately over several vibration periods. The simulation domain is discretized on a $256 \times 170 \times 256$ with $\Delta x = 15/256$
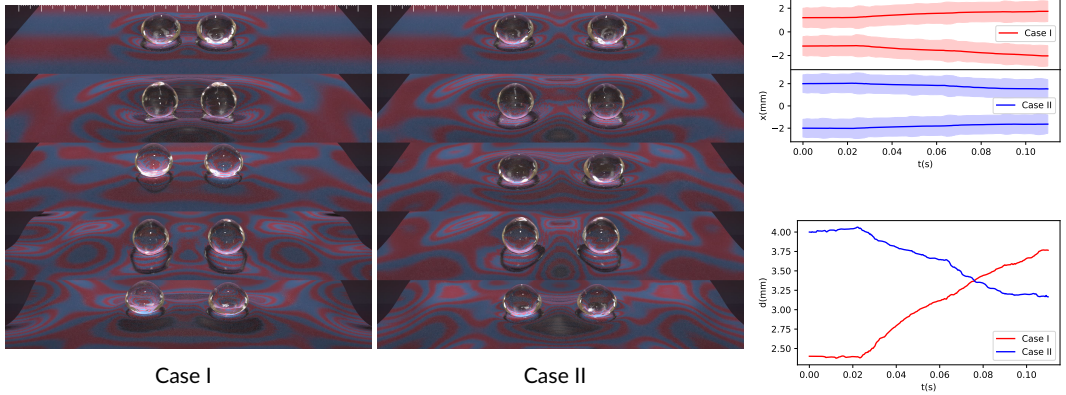
FIGURE 17 *The two droplets bounce on the vibrating bath and form the promenading pairs. Left:* Rendered result for Case I, where two droplets bounce and move away from each other. *Middle:* Rendered result for Case II, where the droplets move towards each other. *Right top:* The droplet positions as a function of time t. The colored stripes indicate the x-axis bounding box of droplets. The solid lines represent the trajectories of the droplet centers. *Right bottom:* The droplet distances as a function of time t.

mm. The time step is $\Delta t = 1 \times 10^{-4}$ s.

The simulation results in Figure 17 show that our method is capable of capturing the interaction between two droplets through the wave field and reproducing two phases of the promenading modes. In Case I, with a small initial droplet distance, two droplets bounce and move away from each other, while in Case II, with a larger distance, they bounce and move towards each other. The trajectories of two droplets and their distances are plotted aside.

In this scene, we demonstrate that our algorithm is compatible with multiple liquid volumes. By using separate field discretization for each liquid volume, minimal modifications are required when applying the algorithm to multiple liquid volumes. In particular, the air film construction and the region topological change step (splitting and merging) are executed sequentially for all possible liquid volume pairs in cases with multiple liquids.
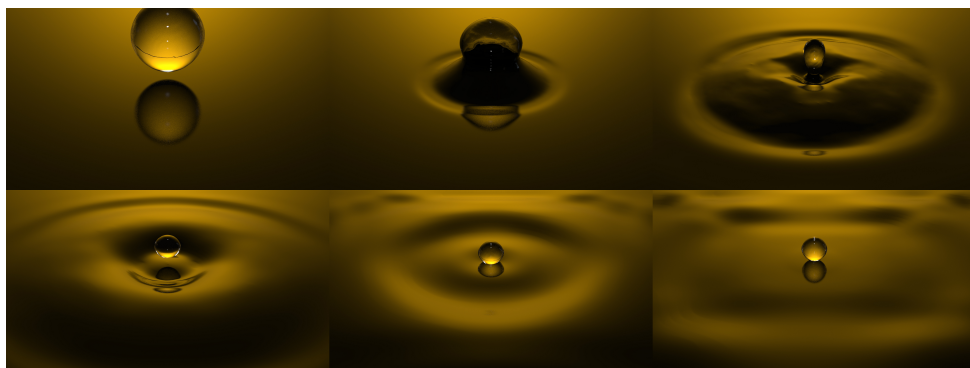
6.6 | Merging and pinching

As shown in 18, we reproduce the droplet pinch-off with a large droplet ($R = 10$ mm) released on a still bath, similar to [23]. When the large droplet touches the liquid bath, it merges with the liquid surface. Following the merging, a thin liquid column emerges, breaks off, and eventually pinches off a small droplet due to the surface tension, which is able to sit on the bath for several seconds.

We simulate the scene with a $256 \times 128 \times 256$ grid with $\Delta x = 120/256$ mm and $\Delta t = 2 \times 10^{-4}$ s. The density of the liquid is $\rho_1 = 949$ kg/m^3 and the surface tension is $\sigma = 1333.3$ mN/m.

When the large droplet touches the liquid bath, the negative thickness correction is turned off to mimic the droplet merging caused by the Van der Waals force. After the droplet merges with the bath, we switch to the semi-implicit surface tension to avoid the numerical viscosity at the thin liquid neck. The weight $w_{exp} = 0.3$ is used for the explicit surface tension part and $w_{imp} = 0.7$ for the implicit part. After the pinch-off, we switch back to the implicit surface tension solver.

The topological changes of the liquid volumes, including splitting and merging, are resolved automatically on the

FIGURE 18 *Droplet merging and pinching*. A large droplet falls and merges with the bath, which causes a thin liquid column to form due to the surface tension. The column eventually breaks off and pinches off a smaller droplet bouncing on the bath.

TABLE 2 Physical parameters in the scenes

Scene	$|g|$(m/s^2)	ρ_1(kg/m^3)	σ_1(mN/m)	ρ_2(kg/m^3)	μ_2(μPas)
Binary Collision (I & II)	–	762	26.56	1	18.6
Trinary Collision	–	762	26.56	1	18.6
Bouncing Droplet	9.8	949	20.6	1	18.6
Promenading Pairs (I & II)	9.8	949	20.6	1	18.6
Merging and Pinching	9.8	949	1333.3	1	18.6

node-based level sets. To detect splitting, we execute the flood fill algorithm on each liquid volume level set. When multiple connected components are found, the fluid region is split and these connected components are converted into new fluid regions, each with its own level set and velocity field sampled from the original liquid volume. Merging of two regions is identified when their level sets overlap. It is detected when a cut vertex on the grid edge of the region $\Omega_{1,j}$ is inside of another region $\Omega_{1,k}$, as indicated by $\phi_k(\boldsymbol{x}) < 0$. The regions are then replaced by a newly merged region, whose level set is constructed as $\phi = \min(\phi_j, \phi_k)$. The velocity field of the merged region is copied from the original regions. Specifically, the velocity on the overlapping face is assigned as the average velocity of two original regions.

6.7 | Performance

The physical parameters of the scenes are summarized in Table 2. All the simulations are performed on a PC with Intel® Xeon® E5-2620 v4 2.10GHz CPU. We use the AMGPCG solver in AMGCL[80] to solve the linear system in the implicit surface tension and pressure projection steps. The simulation configurations and timings are listed in Table 3. All the three-dimensional simulations are rendered using Houdini.

TABLE 3 Simulation configuration and timings

Scene	grid resolution	Δx(mm)	Δt(s)	Iter/Frame	Time/Frame(s)	#DoFs(10^3)
Binary Collision I	$256 \times 128 \times 128$	1/128	5×10^{-6}	1.18	14.37	96.63
Binary Collision II	$256 \times 128 \times 128$	1/128	5×10^{-6}	1.18	14.20	91.85
Trinary Collision	$128 \times 128 \times 128$	1/64	5×10^{-6}	1.00	5.60	19.97
Bouncing Droplet	$256 \times 256 \times 256$	5/256	2×10^{-4}	3.12	128.02	6750.88
Promenading Pairs I	$256 \times 170 \times 256$	15/256	1×10^{-4}	1.16	56.96	5446.76
Promenading Pairs II	$256 \times 170 \times 256$	15/256	1×10^{-4}	1.14	53.28	5448.75
Merging and Pinching	$256 \times 128 \times 256$	15/32	2×10^{-4}	1.19	27.23	2854.92

7 | SUMMARY

This paper proposed a novel computational approach for simulating the bouncing droplet phenomena, with a particular focus on capturing and solving the air film that plays an essential role in fluid collision and coalescing. Based on the cut-cell fluids tracked by separate level sets, we discretize the entrained air film as a single layer of irregular cells that are tightly embedded within the gap formed by adjacent cut-cell fluid interfaces. This allows for efficient handling of the complex film geometry without the need for tedious grid refinement. Building upon this discretization, we model the air film as a thin lubricated layer and couple it with the inviscid incompressible liquid in a monolithic manner. Our method reproduces a wide range of phenomena, including binary collision, bouncing droplets, promenading pairs, and droplet pinch-off, demonstrating its ability to capture many critical dynamical features by accurately resolving the lubricated air flow with liquids.

We identify several limitations and future work directions based on our current approach. *First*, our system does not handle viscosity in the fluid domain. One immediate next step is to add viscosity to the liquid model, which has been proven important in driving droplet walking behaviors [2]. In particular, we plan to focus on the interfacial viscosity coupling between liquid volumes and the air film. *Second*, the physical accuracy of our fluid-fluid coalescence model can be improved. For example, introducing the Van der Waals force into our continuous flow model is an interesting future direction, which will allow the solver to predict the bouncing and coalescence behaviors based on multiscale physical principles. *Third*, due to the computing resolution and boundary conditions, our solver currently cannot model the interfacial wave dynamics accurately, which limits its capability in handling complex drop-wave interactions such as the pilot drop dynamics [35]. In particular, devising a direct numerical solver to reproduce the full-scale dynamics of a walking droplet and further explore its quantum-mechanics connections still remains challenging (and alluring). *Last*, our current model can only handle thin films between fluid volumes. Extending the proposed cut-cell algorithm to facilitate simulations with more complicated physics, e.g., to capture the air gap between droplets and elastic thin sheets, filaments, and fluffy surfaces, will open up new opportunities for this model in accommodating physical simulations in a wider scope.

Acknowledgements

Data Availability Statement

The data that support the findings of this study are available from the corresponding author upon reasonable request.

references

[1] Pan KL, Law CK, Zhou B. Experimental and mechanistic description of merging and bouncing in head-on binary droplet collision. J Appl Phys 2008;103(6):064901. `https://doi.org/10.1063/1.2841055`.

[2] Moláček J, Bush JWM. Drops walking on a vibrating bath: towards a hydrodynamic pilot-wave theory. J Fluid Mech 2013;727:612–647.

[3] Harris DM, Bush JWM. The pilot-wave dynamics of walking droplets. Phys Fluids 2013;25(9):091112. `https://doi.org/10.1063/1.4820128`.

[4] Py C, Reverdy P, Doppler L, Bico J, Roman B, Baroud CN. Capillary Origami: Spontaneous Wrapping of a Droplet with an Elastic Sheet. Phys Rev Lett 2007 Apr;98:156103. `https://link.aps.org/doi/10.1103/PhysRevLett.98.156103`.

[5] Bico J, Reyssat E, Roman B. Elastocapillarity: When Surface Tension Deforms Elastic Solids. Annu Rev Fluid Mech 2018;50(1):629–659. `https://doi.org/10.1146/annurev-fluid-122316-050130`.

[6] Liu J, Wang M, Feng F, Tang A, Le Q, Zhu B. Hydrophobic and Hydrophilic Solid-Fluid Interaction. ACM Trans Graph 2022 nov;41(6). `https://doi.org/10.1145/3550454.3555478`.

[7] Hale J, Akers C. Deceleration of droplets that glide along the free surface of a bath. J Fluid Mech 2016;803:313–331.

[8] Hu DL, Chan B, Bush JW. The hydrodynamics of water strider locomotion. Nature 2003;424(6949):663–666. `https://doi.org/10.1038/nature01793`.

[9] Buckingham R, Bush JW. Fluid polygons. Phys Fluids 2001;13(9):S10–S10.

[10] Zhu B, Quigley E, Cong M, Solomon J, Fedkiw R. Codimensional surface tension flow on simplicial complexes. ACM Trans Graph 2014;33(4):111.

[11] Li HL, Liu HR, Ding H. A fully 3D simulation of fluid-structure interaction with dynamic wetting and contact angle hysteresis. J Comput Phys 2020;420:109709. `https://www.sciencedirect.com/science/article/pii/S0021999120304836`.

[12] Chen X, Yang V. Direct numerical simulation of multiscale flow physics of binary droplet collision. Phys Fluids 2020;32(6):062103. `https://doi.org/10.1063/5.0006695`.

[13] Chubynsky MV, Belousov KI, Lockerby DA, Sprittles JE. Bouncing off the Walls: The Influence of Gas–Kinetic and van der Waals Effects in Drop Impact. Phys Rev Lett 2020 Feb;124:084501. `https://link.aps.org/doi/10.1103/PhysRevLett.124.084501`.

[14] Jiang F, Liu H, Chen X, Tsuji T. A coupled LBM-DEM method for simulating the multiphase fluid-solid interaction problem. J Comput Phys 2022;454:110963. `https://www.sciencedirect.com/science/article/pii/S0021999122000250`.

[15] Liu WB, Ma DJ, Zhang MY, He AM, Liu NS, Wang P. A new surface tension formulation in smoothed particle hydrodynamics for free-surface flows. J Comput Phys 2021;439:110203. `https://www.sciencedirect.com/science/article/pii/S002199912100098X`.

[16] Yang J, Li Y, Kim J. Modified multi-phase diffuse-interface model for compound droplets in contact with solid. J Comput Phys 2023;491:112345. `https://www.sciencedirect.com/science/article/pii/S0021999123004400`.

[17] Xing J, Ruan L, Wang B, Zhu B, Chen B. Position-Based Surface Tension Flow. ACM Trans Graph 2022 nov;41(6). `https://doi.org/10.1145/3550454.3555476`.

[18] Hyde DAB, Gagniere SW, Marquez-Razon A, Teran J. An Implicit Updated Lagrangian Formulation for Liquids with Large Surface Energy. ACM Trans Graph 2020 nov;39(6). https://doi.org/10.1145/3414685.3417845.

[19] Chen J, Kala V, Marquez-Razon A, Gueidon E, Hyde DAB, Teran J. A Momentum-Conserving Implicit Material Point Method for Surface Tension with Contact Angles and Spatial Gradients. ACM Trans Graph 2021 jul;40(4). https://doi.org/10.1145/3450626.3459874.

[20] Deng Y, Wang M, Kong X, Xiong S, Xian Z, Zhu B. A Moving Eulerian-Lagrangian Particle Method for Thin Film and Foam Simulation. ACM Trans Graph 2022 jul;41(4). https://doi.org/10.1145/3528223.3530174.

[21] Couder Y, Fort E, Gautier CH, Boudaoud A. From Bouncing to Floating: Noncoalescence of Drops on a Fluid Bath. Phys Rev Lett 2005 May;94:177801. https://link.aps.org/doi/10.1103/PhysRevLett.94.177801.

[22] Couder Y, Boudaoud A, Protière S, Fort E. Walking droplets, a form of wave-particle duality at macroscopic scale? Europhys News 2010;41(1):14–18. https://doi.org/10.1051/epn/2010101.

[23] Ding H, Li EQ, Zhang FH, Sui Y, Spelt PDM, Thoroddsen ST. Propagation of capillary waves and ejection of small droplets in rapid droplet spreading. J Fluid Mech 2012;697:92–114.

[24] Walker J. Drops of liquid can be made to float on liquid-what enables them to do so. Sci Am 1978;238(6):151.

[25] Rayleigh L. Investigations in Capillarity. Philos Mag 1899;48(293):321–337. https://doi.org/10.1080/14786449908621342.

[26] Zhang P, Law CK. An analysis of head-on droplet collision with large deformation in gaseous medium. Phys Fluids 2011;23(4):042102. https://doi.org/10.1063/1.3580754.

[27] Gilet T, Bush JWM. The fluid trampoline: droplets bouncing on a soap film. J Fluid Mech 2009;625:167–203.

[28] Moláček J, Bush JWM. A quasi-static model of drop impact. Phys Fluids 2012;24(12):127103. https://doi.org/10.1063/1.4771607.

[29] Gilet T, Bush JWM. Droplets bouncing on a wet, inclined surface. Phys Fluids 2012;24(12):122103. https://doi.org/10.1063/1.4771605.

[30] Couder Y, Protière S, Fort E, Boudaoud A. Walking and orbiting droplets. Nature 2005 Sep;437(7056):208–208. https://doi.org/10.1038/437208a.

[31] Couder Y, Fort E. Single-particle diffraction and interference at a macroscopic scale. Phys Rev Lett 2006 Oct;97:154101. https://link.aps.org/doi/10.1103/PhysRevLett.97.154101.

[32] Eddi A, Fort E, Moisy F, Couder Y. Unpredictable Tunneling of a Classical Wave-Particle Association. Phys Rev Lett 2009 Jun;102:240401. https://link.aps.org/doi/10.1103/PhysRevLett.102.240401.

[33] Harris DM, Bush JWM. Droplets walking in a rotating frame: from quantized orbits to multimodal statistics. J Fluid Mech 2014;739:444–464.

[34] Oza AU, Harris DM, Rosales RR, Bush JWM. Pilot-wave dynamics in a rotating frame: on the emergence of orbital quantization. J Fluid Mech 2014;744:404–429.

[35] Bush JWM. Pilot-Wave Hydrodynamics. Annu Rev Fluid Mech 2015;47(1):269–292. https://doi.org/10.1146/annurev-fluid-010814-014506.

[36] Oza AU, Wind-Willassen Ø, Harris DM, Rosales RR, Bush JWM. Pilot-wave hydrodynamics in a rotating frame: Exotic orbits. Phys Fluids 2014;26(8):082101. https://doi.org/10.1063/1.4891568.

[37] Durey M, Milewski PA. Faraday wave–droplet dynamics: discrete–time analysis. J Fluid Mech 2017;821:296–329.

[38] Arbelaiz J, Oza AU, Bush JWM. Promenading pairs of walking droplets: Dynamics and stability. Phys Rev Fluids 2018 Jan;3:013604. `https://link.aps.org/doi/10.1103/PhysRevFluids.3.013604`.

[39] Sáenz PJ, Pucci G, Goujon A, Cristea-Platon T, Dunkel J, Bush JWM. Spin lattices of walking droplets. Phys Rev Fluids 2018 Oct;3:100508. `https://link.aps.org/doi/10.1103/PhysRevFluids.3.100508`.

[40] Couchman MMP, Bush JWM. Free rings of bouncing droplets: stability and dynamics. J Fluid Mech 2020;903:A49.

[41] Bush JWM, Oza AU. Hydrodynamic quantum analogs. Rep Prog Phys 2020 dec;84(1):017001. `https://doi.org/10.1088/1361-6633/abc22c`.

[42] Ando R, Thurey N, Tsuruno R. Preserving fluid sheets with adaptively sampled anisotropic particles. IEEE Trans Vis Comput Graph 2012;18(8):1202–1214.

[43] Batty C, Uribe A, Audoly B, Grinspun E. Discrete viscous sheets. ACM Trans Graph 2012;31(4):113.

[44] Thürey N, Wojtan C, Gross M, Turk G. A Multiscale Approach to Mesh-Based Surface Tension Flows. In: ACM SIGGRAPH 2010 Papers SIGGRAPH '10, New York, NY, USA: Association for Computing Machinery; 2010. .

[45] Zhu B, Lee M, Quigley E, Fedkiw R. Codimensional non-Newtonian fluids. ACM Trans Graph 2015;34(4):115.

[46] Zheng W, Yong JH, Paul JC. Simulation of Bubbles. In: Proc. of ACM SIGGRAPH/Eurographics Symp. on Comput. Anim. SCA '06, Goslar, DEU: Eurographics Association; 2006. p. 325–333.

[47] Da F, Batty C, Wojtan C, Grinspun E. Double bubbles sans toil and trouble: Discrete circulation-preserving vortex sheets for soap films and foams. ACM Trans Graph 2015;34(4):149.

[48] Ishida S, Yamamoto M, Ando R, Hachisuka T. A hyperbolic geometric flow for evolving films and foams. ACM Trans Graph 2017;36(6):199.

[49] Ishida S, Synak P, Narita F, Hachisuka T, Wojtan C. A Model for Soap Film Dynamics with Evolving Thickness. ACM Trans Graph 2020 aug;39(4). `https://doi.org/10.1145/3386569.3392405`.

[50] Wang M, Deng Y, Kong X, Prasad AH, Xiong S, Zhu B. Thin-Film Smoothed Particle Hydrodynamics Fluid. ACM Trans Graph 2021 jul;40(4). `https://doi.org/10.1145/3450626.3459864`.

[51] He X, Wang H, Zhang F, Wang H, Wang G, Zhou K. Robust Simulation of Sparsely Sampled Thin Features in SPH-Based Free Surface Flows. ACM Trans Graph 2015 dec;34(1). `https://doi.org/10.1145/2682630`.

[52] Wang H, Jin Y, Luo A, Yang X, Zhu B. Codimensional Surface Tension Flow Using Moving-Least-Squares Particles. ACM Trans Graph 2020 aug;39(4). `https://doi.org/10.1145/3386569.3392487`.

[53] Wojtan C, Thürey N, Gross M, Turk G. Physics-Inspired Topology Changes for Thin Fluid Features. ACM Trans Graph 2010 jul;29(4). `https://doi.org/10.1145/1778765.1778787`.

[54] Saye RI, Sethian JA. Multiscale Modeling of Membrane Rearrangement, Drainage, and Rupture in Evolving Foams. Science 2013;340(6133):720–724.

[55] Saye RI, Sethian JA. Multiscale modelling of evolving foams. J Comput Phys 2016;315:273–301. `https://www.sciencedirect.com/science/article/pii/S0021999116300158`.

[56] Li J. Macroscopic Model for Head-On Binary Droplet Collisions in a Gaseous Medium. Phys Rev Lett 2016 Nov;117:214502. `https://link.aps.org/doi/10.1103/PhysRevLett.117.214502`.

[57] Hendrix MHW, Bouwhuis W, van der Meer D, Lohse D, Snoeijer JH. Universal mechanism for air entrainment during liquid impact. J Fluid Mech 2016;789:708–725.

[58] Liu M, Bothe D. Toward the predictive simulation of bouncing versus coalescence in binary droplet collisions. Acta Mech 2019;230(2):623–644. https://doi.org/10.1007/s00707-018-2290-4.

[59] Musehane NM, Oxtoby OF, Reddy BD. Multi-scale simulation of droplet–droplet interaction and coalescence. J Comput Phys 2018;373:924–939. https://www.sciencedirect.com/science/article/pii/S0021999118304881.

[60] Batty C, Bertails F, Bridson R. A Fast Variational Framework for Accurate Solid-Fluid Coupling. ACM Trans Graph 2007 jul;26(3):100–es. https://doi.org/10.1145/1276377.1276502.

[61] Ng YT, Min C, Gibou F. An efficient fluid–solid coupling algorithm for single-phase flows. J Comput Phys 2009;228(23):8807–8829. https://www.sciencedirect.com/science/article/pii/S0021999109004719.

[62] Edwards E, Bridson R. Detailed Water with Coarse Grids: Combining Surface Meshes and Adaptive Discontinuous Galerkin. ACM Trans Graph 2014 jul;33(4). https://doi.org/10.1145/2601097.2601167.

[63] Quan S, Lou J, Schmidt DP. Modeling merging and breakup in the moving mesh interface tracking method for multiphase flow simulations. J Comput Phys 2009;228(7):2660–2675. https://www.sciencedirect.com/science/article/pii/S002199910800675X.

[64] Chen X, Yang V. Thickness-based adaptive mesh refinement methods for multi-phase flow simulations with thin regions. J Comput Phys 2014;269:22–39. https://www.sciencedirect.com/science/article/pii/S0021999114001612.

[65] Qiu L, Yu Y, Fedkiw R. On thin gaps between rigid bodies two-way coupled to incompressible flow. J Comput Phys 2015;292:1–29. https://www.sciencedirect.com/science/article/pii/S0021999115001746.

[66] Azevedo VC, Batty C, Oliveira MM. Preserving Geometry and Topology for Fluid Flows with Thin Obstacles and Narrow Gaps. ACM Trans Graph 2016 jul;35(4). https://doi.org/10.1145/2897824.2925919.

[67] Li W, Ma Y, Liu X, Desbrun M. Efficient Kinetic Simulation of Two-Phase Flows. ACM Trans Graph 2022 jul;41(4). https://doi.org/10.1145/3528223.3530132.

[68] Takahashi T, Lin MC. A Geometrically Consistent Viscous Fluid Solver with Two-Way Fluid-Solid Coupling. Comput Graph Forum 2019;38(2):49–58. https://onlinelibrary.wiley.com/doi/abs/10.1111/cgf.13618.

[69] Zarifi O, Batty C. A Positive-Definite Cut-Cell Method for Strong Two-Way Coupling between Fluids and Deformable Bodies. In: Proc. of ACM SIGGRAPH/Eurographics Symp. on Comput. Anim. SCA '17, New York, NY, USA: Association for Computing Machinery; 2017. .

[70] Chen YL, Meier J, Solenthaler B, Azevedo VC. An Extended Cut-Cell Method for Sub-Grid Liquids Tracking with Surface Tension. ACM Trans Graph 2020 nov;39(6). https://doi.org/10.1145/3414685.3417859.

[71] Brochu T, Batty C, Bridson R. Matching Fluid Simulation Elements to Surface Geometry and Topology. ACM Trans Graph 2010 jul;29(4). https://doi.org/10.1145/1778765.1778784.

[72] Gibou F, Hyde D, Fedkiw R. Sharp interface approaches and deep learning techniques for multiphase flows. J Comput Phys 2019;380:442–463. https://www.sciencedirect.com/science/article/pii/S0021999118303371.

[73] Batty C, Xenos S, Houston B. Tetrahedral Embedded Boundary Methods for Accurate and Flexible Adaptive Fluids. Comput Graph Forum 2010;29(2):695–704. https://onlinelibrary.wiley.com/doi/abs/10.1111/j.1467-8659.2009.01639.x.

[74] Xiao Y, Chan S, Wang S, Zhu B, Yang X. An Adaptive Staggered-Tilted Grid for Incompressible Flow Simulation. ACM Trans Graph 2020 nov;39(6). https://doi.org/10.1145/3414685.3417837.

[75] Smith FT, Li L, Wu GX. Air cushioning with a lubrication/inviscid balance. J Fluid Mech 2003;482:291–318.

[76] Hamrock BJ, Schmid SR, Jacobson BO. Fundamentals of fluid film lubrication. CRC press; 2004.

[77] Lorensen WE, Cline HE. Marching Cubes: A High Resolution 3D Surface Construction Algorithm. SIGGRAPH Comput Graph 1987 aug;21(4):163–169. `https://doi.org/10.1145/37402.37422`.

[78] Kim B, Liu Y, Llamas I, Jiao X, Rossignac J. Simulation of Bubbles in Foam with the Volume Control Method. ACM Trans Graph 2007 jul;26(3):98–es. `https://doi.org/10.1145/1276377.1276500`.

[79] Selle A, Fedkiw R, Kim B, Liu Y, Rossignac J. An Unconditionally Stable MacCormack Method. J Sci Comput 2008 Jun;35(2):350–371. `https://doi.org/10.1007/s10915-007-9166-4`.

[80] Demidov D. AMGCL – A C++ library for efficient solution of large sparse linear systems. Software Impacts 2020;6:100037. `https://doi.org/10.1016/j.simpa.2020.100037`.

A | LUBRICATION MODEL IN THE AIR FILM

As two liquid regions approach each other, the thickness of inter-liquid film between them decreases. The dimension of the film in the normal direction becomes much smaller than its dimension in the tangential direction, and the viscosity drag becomes the dominant force. Through order analysis, we model the air flow in the gap using the lubrication theory[75].

In the lubricated film, the normal and tangent gradient of the air pressure are modeled as

$$
\begin{cases}
\dfrac{\partial p_2}{\partial \xi_t} = \mu_2 \dfrac{\partial^2 u_t}{\partial \xi_n^2}, \\[2mm]
\dfrac{\partial p_2}{\partial \xi_n} = 0,
\end{cases}
\quad \boldsymbol{x} \in \Omega_2,
\tag{14}
$$

with

$$
\begin{cases}
[p_2] = -\gamma\kappa, \quad \boldsymbol{x} \in \Gamma_{12}, \\[2mm]
[p_2] = 0, \quad \boldsymbol{x} \in \Gamma_{23}.
\end{cases}
\tag{15}
$$

where ξ_n and ξ_t denote the local unit normal and tangent directions, respectively, u_n, u_t are normal and tangent components of the air velocity, respectively.

To derive the equation that updates the tangential velocity by the pressure gradient, we integrate the first equation in Equation 14 with respect to the normal direction ξ_n:

$$
\xi_n \frac{\partial p}{\partial \xi_t} = \mu \left(\frac{\partial u_t}{\partial \xi_n} - \frac{\partial u_t}{\partial \xi_n}\big|_{\xi_n=0} \right)
\tag{16}
$$

Then we integrate it again on the intervals $[0, \xi_n]$ and $[0, h]$ (h is the thickness of the air film):

$$
\begin{aligned}
\frac{\xi_n^2}{2} \frac{\partial p}{\partial \xi_t} &= \mu \left(u_t(\xi_n) - u_t(0) - \xi_n \frac{\partial u_t}{\partial \xi_n}\big|_{\xi_n=0} \right) \\[2mm]
\frac{h^2}{2} \frac{\partial p}{\partial \xi_t} &= \mu \left(u_t(h) - u_t(0) - h \frac{\partial u_t}{\partial \xi_n}\big|_{\xi_n=0} \right)
\end{aligned}
\tag{17}
$$

By combining these two equations to eliminate $\frac{\partial u_t}{\partial \xi_n}|_{\xi_n=0}$ and applying the boundary conditions $u_t(h) = u_{t\uparrow}, u_t(0) = u_{t\downarrow}$, the tangential velocity of the air film is given as:

$$u_t(\xi_n) = -\xi_n \frac{h-\xi_n}{2\mu} \frac{\partial p}{\partial \xi_t} + \frac{h-\xi_n}{h} u_{t\downarrow} + \frac{\xi_n}{h} u_{t\uparrow} \tag{18}$$

The average tangent velocity of the film can be obtained by integrating the tangent velocity from $\xi_n = 0$ to $\xi_n = h$

$$
\begin{aligned}
hu_t^* &= \int_0^h u_t(\xi_n) d\xi_n \\
&= \int_0^h \left(-\xi_n \frac{h-\xi_n}{2\mu} \frac{\partial p}{\partial \xi_t} + \frac{h-\xi_n}{h} u_{t\downarrow} + \frac{\xi_n}{h} u_{t\uparrow} \right) d\xi_n \\
&= \left(-\frac{\xi_n^2 h}{4\mu} \frac{\partial p}{\partial \xi_t} + \frac{\xi_n^3}{6\mu} \frac{\partial p}{\partial x} + \xi_n u_{t\downarrow} + \frac{\xi_n^2}{h}(u_{t\uparrow} - u_{t\downarrow}) \right) \Big|_0^h \\
&= \frac{h^3}{12\mu} \frac{\partial p}{\partial \xi_t} + \frac{h}{2}(u_{t\uparrow} + u_{t\downarrow})
\end{aligned}
\tag{19}
$$

Thus the average tangent velocity of the air film is

$$u_t^* = -\frac{h^2}{12\mu} \frac{\partial p}{\partial \xi_t} + \frac{1}{2} u_{t\uparrow} + \frac{1}{2} u_{t\downarrow} \tag{20}$$

In the normal direction, the velocity on the interface Γ_{12} is updated by the pressure gradient across the liquid and the air.

$$u_n^* = u_n - \frac{\Delta t}{\rho_2} \frac{\partial p_2}{\partial \xi_n}, \boldsymbol{x} \in \Gamma_{12} \tag{21}$$

Given a volume V in the air film with its tangent boundary ∂V_t and normal boundary $\partial V_s \subseteq \Gamma_{12}$, the incompressibility is achieved by summing up the integrated flow through the boundary:

$$\int_{\partial V_t} u_t^* ds + \int_{\partial V_n} u_n^* ds = 0 \tag{22}$$

Substituting Equation (20) and (21) into it yields the reduced model for the air film:

$$\int_{\partial V_t} \frac{h^2}{12\mu} \frac{\partial p_2}{\partial \xi_t} ds + \Delta t \int_{\partial V_n} \frac{1}{\rho_2} \frac{\partial p_2}{\partial \xi_n} ds = \int_{\partial V_t} \frac{u_{t\uparrow} + u_{t\downarrow}}{2} ds + \int_{\partial V_n} u_n ds \tag{23}$$

with

$$\begin{cases} [p_2] = -\gamma\kappa, & x \in \Gamma_{12}, \\ [p_2] = 0, & x \in \Gamma_{23}. \end{cases} \tag{24}$$